

CEP-IP: An Explainable Framework for Cell Subpopulation Identification in Single-cell Transcriptomics

Kah Keng Wong

Department of Immunology, School of Medical Sciences, Universiti Sains Malaysia,
16150 Kubang Kerian, Kelantan, Malaysia

TRPM4 is overexpressed in prostate cancer (PCa) associated with metastasis or recurrence. There is paucity of information pertaining to TRPM4 characterization and functions at single-cell level in PCa. This study introduces the CEP-IP framework, a novel explainable machine learning approach for the identification of biologically relevant cell subpopulations in single-cell transcriptomics of pairwise genes. The framework combines cell explanatory power (CEP) classification with inflection point (IP) analysis to assign model performance into individual cells, while stratifying transcriptional space into distinct regions. To demonstrate the CEP-IP framework, generalized additive model (GAM) was applied to model relationships between *TRPM4* and co-expressed genes in aggressive PCa and benign prostate cells from scRNA-seq data. Genes were identified using Spearman–Kendall's dual-filter ($r_s > 0.6$ and $\tau > 0.5$). Seven ribosomal genes (*RPL10*, *RPL27*, *RPL28*, *RPS2*, *RPS8*, *RPS12*, *RPS26*; averaged as Ribo gene set) passed dual-filtering specifically in PCa cells. *TRPM4*-Ribo modeling outperformed alternative cancer gene sets (deviance explained $FDR < 0.05$). The CEP-IP framework identified top-ranked explanatory power (TREP) cells and stratified them using IP analysis into pre-IP and post-IP regions, creating four distinct cell subpopulations per patient. Gene Ontology analysis revealed pre-IP TREP cells enriched for immune-related processes, while post-IP TREP cells enriched for ribosomal, translation, and cell adhesion pathways. In conclusion, the explainable CEP-IP framework allows for the identification of cancer cell subpopulations with distinctive biology and therapeutic implications, applicable to any pairwise gene analysis.

Keywords: Generalized additive model; *TRPM4*; ribosome; cell explanatory power; explainable AI.

1. Introduction

Prostate cancer (PCa) is one of the most commonly diagnosed cancer, a predominant cancer type in elderly men with increasing incidence, and the second highest cancer-related mortality in males [1, 2]. While the five-year overall survival for PCa cases has improved to approximately 90% [3], aggressive PCa characterized by metastasis confers five-year survival rate of 30% [1, 4, 5], highlighting the ongoing needs to improve the outcomes of invasive PCa.

Transient receptor potential melastatin 4 (TRPM4), a member of the TRP superfamily, is a Ca^{2+} -activated, non-selective cation channel that is impermeable to Ca^{2+} but transports monovalent cations including Na^+ and K^+ [6, 7]. TRPM4 has multiple physiological roles, particularly in regulating the physiological processes of cardiac tissues [8-11]. TRPM4 is overexpressed in multiple cancer types such as breast cancer [12, 13], lymphomas [14, 15], and PCa [16-18]. TRPM4 is an established oncogene in PCa as the ion channel is required for PCa tumor growth and their aggressive phenotypes including extravasation, invasion, and metastasis [19-22]. In particular, higher TRPM4 protein expression is associated with metastatic progression of PCa patients [23] and increased risk of biochemical recurrence in PCa [17]. There is lack of single-cell RNA sequencing (scRNA-seq) analysis of *TRPM4* expression and its potential functions at single-cell level in PCa cases.

Generalized additive model (GAM) is an extension of generalized linear models where it models non-linear relationships between predictors and response variable, through the use of flexible splines [24-26]. The splines' flexibility allows modeling of numerous types of predictor-responder relationship, and GAM is widely used in various fields such as environmental sciences [27-29], engineering [30, 31], public health and biomedicine [32-34]. GAMs have also been utilized for scRNA-seq analysis, particularly for cell trajectory analysis [35, 36], attributable to GAM's strengths in modeling non-linear relationships of continuous variables without assuming predetermined functional forms.

However, conventional GAM applications lack methods for assigning overall model performance into the level of individual data points. Moreover, certain newer methods for cell subpopulation identification rely on black-box algorithms that may not be as explainable as GAMs. This explainability gap represents a challenge in explainable artificial intelligence (XAI) applications in medicine, where mapping for the specific cancer cells that drive model predictions is key for therapeutic targeting.

In this study, the potential functions of *TRPM4* at single-cell level was investigated in scRNA-seq dataset of invasive PCa patients (GSE185344) [37]. By leveraging the flexibility and explainability of GAMs, *TRPM4* and its potential response variables were modeled, with specific focus on optimizing the GAM models, mapping for individual cells with strong *TRPM4*-responder relationship to identify their distinct biological features, as well as the explainability of GAMs. Through the transparent and explainable GAM modeling, this study presents the cell explanatory power with inflection point (CEP-IP) framework, a novel explainable machine learning (ML) technique that assigns GAM performance into individual cell contributions. The framework introduces cell explanatory power (CEP) that determines which cells are best predicted by the model, combined with inflection point (IP) analysis that stratifies transcriptional space into biologically distinct quadrants. This CEP-IP framework shows model explainability that aligns with XAI principles, while allowing the identification of cell subpopulations with potential therapeutic relevance.

2. Materials and Methods

2.1 scRNA-seq dataset processing workflow

The scRNA-seq dataset of invasive and intraductal cribriform PCa cases (n=7) with matched non-cancerous samples (NonCa; n=7) of benign-enriched prostate cells (BP), annotated by the original study [37] as HYW_4701 (assigned as Pt.1 in this study), HYW_4847 (Pt.2), HYW_4880 (Pt.3), HYW_4881 (Pt.4), HYW_5386 (Pt.5), HYW_5742 (Pt.6), and HYW_5755 (Pt.7), were obtained from Gene Expression Omnibus (GSE185344).

Standard Seurat processing workflow was performed [38, 39], and multiple quality control (QC) steps were performed to exclude low quality cells before downstream modeling analysis. Initially, cells with <500 unique genes expression were removed. Ribosomal gene filtering was then conducted by mapping for ribosomal genes with RP or MRP prefixes, before excluding top 10% of cells with the highest ribosomal content, minimizing potential bias in downstream analysis introduced by cells with high ribosomal expression. Next, mitochondrial gene filtering was performed by identifying genes with MT- prefix for the exclusion of top 10% of cells with highest mitochondrial content, filtering out stressed or dying cells. Cell cycle effects were then regressed out to remove cell cycle-driven variation that can compromise the main biological signals.

Doublets were then removed using scDblFinder algorithm that identified potential doublets for exclusion. The number of cells before and after each of these QC steps are detailed in **Supplementary Table 1**. Batch effects correction was then conducted using the SCTransform function as the final QC step. Subsequently, dimensionality reduction was performed using principal component analysis (PCA) and uniform manifold approximation and projection (UMAP). This enabled clustering analysis by constructing k-nearest neighbor graph, and for

the identification of the top 50 markers representing each cluster (**Supplementary Table 1**) using the `FindAllMarkers` function. The top markers for each individual cluster were then utilized to determine the cell type according to the enrichment of the Coexpression, Coexpression Atlas, and ToppCell Atlas gene sets available on the ToppGene database [40]. UMAP plots for both PCa and BP cells, with annotated cluster numbers or according to *TRPM4* expression levels, were generated.

2.2 Features selection for GAM modeling and CEP-IP framework

Genome-wide correlation analysis was conducted using Spearman's r_s or Kendall's τ correlation with the base R function `cor()`, of BP cluster 3 (from NonCa cases) versus all PCa clusters 0-22 (from PCa cases), and of PCa clusters versus each other clusters. In addition, r_s and τ correlation analysis of *TRPM4* with all genes was conducted in clusters 6, 9, 11, 14, and 19 combined in the PCa cases, and in cluster 3 (BP cells) from the NonCa cases, in pre-integration Seurat objects to avoid potential batch correction artifacts that may influence correlation patterns. Computation for Kendall's τ was accelerated utilizing 23 CPU cores (Intel Core i9-14900KF) by using the `doParallel` package. Genes that passed the correlation dual-filter, $r_s > 0.6$ and $\tau > 0.5$, were shortlisted for gene set enrichment analysis. The selected features are critical for subsequent CEP-IP framework application to identify therapeutically relevant cell subpopulations.

Heatmap to compare the expression of the seven dual-filtered ribosomal (*RPL10*, *RPL27*, *RPL28*, *RPS2*, *RPS8*, *RPS12*, and *RPS26*) and seven AR-related (*KLK4*, *KLK2*, *KLK3*, *PDLIM5*, *ABHD2*, *ALDH1A3*, and *SORD*) genes, as well as each of the seven genes' averaged expression representatives termed as Ribo and AR in this study, in PCa and NonCa clusters. In each cluster, cells were ordered according to ascending *TRPM4* expression level. Expression was represented as z-score using the mako palette of the `viridis` package.

In order to assess whether averaging the expression of the seven ribosomal or AR genes was suitable for downstream modeling, the internal reliability of these two gene sets was assessed for PCa and NonCa cases. For each sample and gene set combination, the consistency among individual genes within the averaged gene set was tested. The metrics used for the evaluation were Cronbach's alpha (α), McDonald's omega (ω), and the Kaiser-Meyer-Olkin (KMO) measure of sampling adequacy, using the `psych` package. A consolidated score (CS score) was calculated by averaging the values of these three metrics.

2.3 Optimization and explainability of *TRPM4*-ribosomal (*TRPM4*-Ribo) relationship modeling with GAM

Modeling with GAM was conducted using the `mgcv` package [26, 41, 42]. The GAM model was initialized to take in the form $f(x_i) = \beta_0 + \beta_1 x_i + b_1 \varphi_1(x_i) + \dots + b_n \varphi_n(x_i)$ where each cell's *TRPM4* value x_i was implemented to predict the expression value $f(x_i)$ of seven gene sets separately (i.e., Ribo, AR, GSK-3 β , mTOR, NF- κ B, PI3K/AKT, and Wnt, with the Ribo and AR gene sets utilized for optimization and explainability). Optimization steps were conducted for the modeling to minimize potential overfitting or underfitting of the fitted GAM curve.

To achieve this, selection of the k value (maximum number of smooth basis functions) was optimized by minimizing penalized residual sum of squares (PRSS) via two phases i.e., initial exploration phase (PRSS iterations 1–8), and convergence verification phase (PRSS iterations 9 up to maximum 100 with early stopping). In the exploration phase, cells were extracted from specific clusters (e.g., the five PCa clusters 6, 9, 11, 14, and 19) and samples (e.g., PCa samples) using Seurat objects, and average gene set expression versus *TRPM4* expression were calculated before \log_2 transformation of the expression values.

Then, the exploration phase tested different k values ($k=3-10$) in the first eight iterations, followed by PRSS convergence verification phase that alternated between using the best k

value and sampling from neighboring k values (± 1 of best k) for up to 92 iterations. The alternation occurred every third iteration (i.e., iterations 9, 12, 15, etc. sampled randomly from the ± 1 range, while other iterations used the best k value). Early stopping was initiated if no improvement in PRSS value was observed for 20 consecutive iterations, indicating PRSS value convergence. The key lines of code illustrating the exploration of k values in both phases of PRSS optimization are as follows:

```
# Exploration phase: In the first eight iterations, explore k values
# ranging from 3 to 10
max_k <- min(10, unique_trpm4 - 1)
k <- 3 + ((i - 1) %% (max_k - 2))

# PRSS convergence verification phase: Up to 92 iterations (iterations
# no. 9 to 100), tested random  $\pm 1$  best k value every third iteration,
# early stopping after 20 consecutive iterations without PRSS
# improvement
if (best_k == max_k) {
  k_range <- c(max_k - 1, max_k)
} else if (best_k == 3) {
  k_range <- c(3, 4)
} else {
  k_range <- c(best_k - 1, best_k, best_k + 1)
}

# Try best_k $\pm 1$  range every third iteration
if (i %% 3 == 0) {
  k <- sample(k_range, 1)
} else {
  k <- best_k
}
```

In each PRSS iteration, GAM was fitted using thin-plate regression spline (TPRS). For each PRSS iteration, the fitted spline was penalized by the smoothing parameter λ derived from restricted maximum likelihood (REML). Hence, PRSS was the outer loop (running both the exploration and verification phases described earlier, where the lowest PRSS value yielded the best k value) and REML was the inner loop (where the lowest REML score yielded the best λ value) in the optimization process to yield optimal GAM fitting. For each PRSS iteration (outer loop), the PRSS iteration number, PRSS value, k value, REML iteration count, and final REML score, were captured. The summarized code is as follows:

```
# PRSS and REML as the outer and inner Loop, respectively
for (i in 1:num_iterations) {
  # Fit GAM model with PRSS-optimized k value
  gam_model <- gam(Expression ~ TRPM4 + s(TRPM4, bs = "tp", k = k),
    data = sample_data, method = "REML", select = TRUE, gamma = 1.5)

  # Calculate PRSS for outer Loop optimization
  prss_components <- calculate_prss(gam_model, sample_data)
  current_prss <- prss_components$PRSS
}
```

For each REML iteration (inner loop), the REML score, λ value, iteration number, REML convergence, gradient and Hessian values were extracted. Gradient extraction was achieved

by accessing `model$outer.info$grad`, where `mgcv` stored the first three iterations. Hessian extraction was challenging as `mgcv` stored only the final convergence Hessian and not for earlier REML iterations during REML optimization. To address this, inverse Hessian (H^{-1}) value was backcalculated using the Newton–Raphson method by utilizing the rest of the available components including the initial λ value (λ_{old}), its consecutive λ value (λ_{new}), and gradient value. Using the Newton–Raphson method formula $\log(\lambda_{\text{new}}) = \log(\lambda_{\text{old}}) - H^{-1}g$, the inverse Hessian was backcalculated as $H^{-1} = (\log(\lambda_{\text{old}}) - \log(\lambda_{\text{new}}))/g$

For REML, monotonic decrease in REML score across iterations was assessed to verify that REML score reduced with each successive iteration. In addition, REML convergence was determined by either of these criteria:

- i) Maximum number of iterations reached, following the default set by `model$control$maxit`
- ii) Gradient-based convergence: when gradient norm (GN) fell below threshold ($<1 \times 10^{-5}$).
- iii) Score-based convergence: when relative REML score change dropped below threshold ($<1 \times 10^{-6}$).
- iv) Fallback convergence: when `mgcv` reported convergence for reasons other than the aforementioned.

The PRSS and REML optimization processes were visualized in line plots showing how their values changed across iterations, and their convergence. For the best model (*i.e.*, fitted with k and λ derived from the best PRSS iteration), multiple model information was extracted including each cell's coefficient values for the linear and smooth terms (*i.e.*, spline basis functions φ_1, φ_2 , etc.), the knot locations, model and null deviances, smooth terms' effective degrees of freedom and their p -values adjusted for multiple testing by the Benjamini–Hochberg method (false discovery rate, FDR), testing the significance of non-linear relationships, individual cell-level *TRPM4* expression, and gene set expression values (actual or predicted values by the model).

Multi-gene set analysis was performed in batch for all samples. The fitted full model of the relationship between *TRPM4* expression (x-axis, \log_2 scale) and various gene sets (Ribo, AR, GSK-3 β , mTOR, NF- κ B, PI3K/AKT, and Wnt; y-axis, \log_2 scale) was visualized in scatter plots with fitted GAM curves. To adjust for optimal smoothness of the fitted curves, the γ parameter in REML that controls penalization of smooth terms was tested in 0.5 increments (γ range tested: 0.5–3.0), and the resulting GAM curves were visually inspected for signs of overfitting, underfitting, or optimal model fit.

2.4 Visualization of TPRS basis functions formation

To visualize the smooth basis functions (TPRS) formation, *TRPM4*-Ribo modeling in Pt.4 was used as the representative and GAM fitting was performed with optimized parameters ($k=10$, $\lambda=0.528$). Initially, basic statistical analysis (*e.g.*, data distribution) was demonstrated before showing representative knots for the formation of radial basis functions into actual spline shapes. Individual smooth basis functions (φ_1 – φ_8) in unpenalized forms were then extracted from the model's prediction matrix. Coefficients were applied, yielding penalized smooth basis functions that were then cumulatively combined to demonstrate how the complete smooth terms (φ_1 – φ_8 combined) differed from those with incomplete smooth basis functions (*e.g.*, φ_1 and φ_8 only).

The final GAM curve was formed by adding complete smooth terms with the linear terms, and three data points with low (5th percentile), medium (50th percentile), and high (95th percentile) *TRPM4* values were selected as representatives for the calculation of the full model's predicted Ribo expression values. The variance contribution of each term to the full model was extracted to compare the magnitude of their contributions to the model.

2.5 CEP-IP framework: The CEP classification

The CEP-IP framework was developed and introduced here to identify biologically distinct cell subpopulations. This was achieved by combining the CEP classification for identifying well-predicted cells, and IP analysis for spatial stratification of transcriptional space. Deviance explained (DE) was the performance metrics used in this study to measure how much of variability in a specific gene set's expression was captured by *TRPM4*. As the spline in GAM was fitted according to the distribution of cells in *TRPM4*-gene set transcriptional space, specific cells with strong *TRPM4*-gene set relationship would be well-predicted by the fitted model, and this population of cells may be biologically relevant. Hence, attempts to decompose DE into cell-level were conducted, where Gaussian GAM's DE aggregate sums were decomposed into cell-level consisting of null deviance contribution (NDC), model deviance contribution (MDC), and explanatory power (EP) as follows:

DE (Gaussian GAM):

$$\begin{aligned} \text{Null deviance (ND)} &= \sum (y_i - \bar{y})^2 && (\text{sum of squared null residuals from all cells}) \\ \text{Model deviance (MD)} &= \sum (y_i - f(x_i))^2 && (\text{sum of squared model residuals from all cells}) \\ \text{DE} &= 1 - (\text{MD} / \text{ND}) && (\text{proportion of variability explained by the model}) \end{aligned}$$

EP:

$$\begin{aligned} \text{NDC}_i &= (y_i - \bar{y})^2 && (i\text{-th cell ND contribution}) \\ \text{MDC}_i &= (y_i - f(x_i))^2 && (i\text{-th cell MD contribution}) \\ \text{EP}_i &= 1 - (\text{MDC}_i / \text{NDC}_i) && (\text{proportion of } i\text{-th cell-level variability explained}) \end{aligned}$$

When all individual cell's EP had been computed, the cells were then ranked according to EP values from the highest to the lowest. Based on this ranking, the top DE% were selected as top-ranked EP (TREP) cells. For instance, if total of 100 cells and DE was 45%, then cells ranked first to 45th by EP were assigned as TREP cells, while cells ranked 46th to 100th were non-TREP cells. When DE resulted in fractional cell numbers (e.g., DE=45.6% with 100 cells), the exact number was determined by rounding $n \times \text{DE}$ to the nearest integer.

2.6 CEP-IP framework: Monte Carlo cross-validation (MCCV) of CEP classification

To validate the accuracy of CEP classification in decomposing DE into cell-level assignment of TREP and non-TREP cells, MCCV was conducted where PCa cells of each patient were divided into training: test sets in 70:30 ratio for 20 randomized iterations. In the training set, the optimal *TRPM4*-Ribo GAM model determined from prior analysis (with optimized k , λ , and γ derived from the minimized PRSS, REML, and GAM curves visual inspection, respectively) was fitted for each case. The cells were then CEP-classified into TREP and non-TREP as described previously *i.e.*, according to EP and DE values.

In the test set, the trained GAM model was applied to predict the Ribo values of the cells required to generate their EP values, and training set's DE was then applied to binarize test set cells into TREP and non-TREP. Root mean squared error (RMSE) was calculated for both TREP and non-TREP groups, where each cell's actual versus predicted Ribo value residuals were computed, and RMSE was the square root of the mean of TREP (or non-TREP) cells' squared residuals $[(\text{mean}(\text{test_residuals}[\text{TREP_cells}]^2))^{1/2}]$. Difference in the RMSE values for both TREP and non-TREP groups were then computed. Significance of the RMSE differences between both groups across 20 iterations was computed using one-sample t-test (against a null hypothesis of zero RMSE difference) or Wilcoxon signed-rank test if RMSE differences had normal or non-normal distribution, respectively, using Shapiro-Wilk test.

For comparison with negative controls, the cells were randomly assigned as TREP and non-TREP cells (maintaining the same proportion as the training set's DE) instead of CEP classification and underwent identical analysis. For comparison with an additional control group, leverage-based classification was adopted to assign cells into TREP and non-TREP,

whereby statistical leverage (hat values) was first computed to generate influence scores [combination of leverage and standardized residuals, $\text{influence_score} = (\text{leverage} \times \text{standardized_residuals}^2)^{1/2}$] used to rank the cells, replacing EP-based ranking before selecting the top DE% as leverage-based TREP cells. Downstream RMSE calculations and comparisons between both cell groups for random or leverage-based classification were computed as described above for CEP-based classification.

2.7 CEP-IP framework: Spatial stratification with IP analysis, distribution pattern, and Gene Ontology (GO) analysis of cell subpopulations

Inflection point (IP) in a GAM plot represented the *TRPM4* expression value, determined visually, where distribution pattern of CEP-classified TREP cells (colored in purple; non-TREP cells colored in gray) shifted near the midpoint of *TRPM4* expression range, where the number of TREP cells were immediately more above the GAM curve. IP binarized the GAM plot into the pre-IP (*TRPM4*<IP) and post-IP (*TRPM4*≥IP) regions on the x-axis scale (*TRPM4* expression). Pre-IP was characterized by a pattern of decreasing TREP cells frequency toward the IP, while the post-IP region exhibited increasing frequency of TREP cells away from the IP. Differences in the proportion of TREP versus non-TREP cells above and below the GAM curve was assessed using chi-square test or Fisher's exact test (when any expected count was <5 in the contingency table), adjusted by FDR and represented in mosaic plots. Ribo values of pre-IP cells were compared with post-IP cells in raincloud plots, and overlap between both regions was compared using overlap coefficient (OVL).

Differential gene expression (DEG) analysis was performed in TREP versus non-TREP cells within pre-IP or post-IP regions separately, using Seurat's FindMarkers function with Wilcoxon rank-sum tests. DEG detection required at least 10% gene expression frequency, \log_2 fold-change ($\log_2\text{FC}$) threshold of 0.1, and minimum three cells per comparison group. DEGs with $p<0.01$ and $\log_2\text{FC}>0.2$ were shortlisted for further analysis, except in Pt.5 adopting DEGs with $p<0.05$ and $\log_2\text{FC}>0.1$ due to insufficient DEGs for downstream analysis with prior thresholds. For cases with >500 shortlisted DEGs, the top 500 DEGs ranked according to the most significant p -values were selected to avoid false positives beyond 500 DEGs. GO enrichment analysis was performed using the ToppGene platform with the full gene set used as the background gene set. Each patient's pre-IP and post-IP regions consisted of GOs upregulated in TREP or non-TREP cells. The top 50 GOs with $\text{FDR}<0.05$ were shortlisted. GOs with similar annotations were compiled into a consensus functional group, and GO with the most significant FDR within a functional group was selected for comparison with other functional groups' most significant GO.

2.8 CEP-IP framework: Monocle3 trajectory analysis of mapped TREP and non-TREP cells

Seurat-processed PCa and NonCa objects were converted to Monocle3 format for trajectory analysis, followed by dimensionality reduction with PCA and UMAP embedding. Trajectory roots were defined as cells with the highest *TRPM4* expression, and cells were clustered with trajectory graphs. Pseudotime ordering was performed to capture cellular transitions along the learned trajectories. Quantitative assessment of TREP cells separation between pre-IP and post-IP regions, in terms of UMAP1 coordinate distributions, was performed using t-test (normal distribution) or Mann-Whitney U test (non-normally distributed data) with Cliff's delta (δ) effect size estimation. Ridgeline plots were generated to visualize UMAP1 coordinate distributions across all four cell groups (pre-IP TREP, pre-IP non-TREP, post-IP TREP, post-IP non-TREP), and p -values of the UMAP1 comparisons between both regions (pre-IP versus post-IP) were computed and FDR-corrected for all patients.

2.9 Statistical analysis

The Shapiro-Wilk test was conducted to test normality of the distribution of continuous variables. For comparison of continuous variables between two groups, t-test or Mann-Whitney U test was conducted for normal or non-normally distributed data, respectively. For

continuous variables' comparison between more than two groups, ANOVA with Holm-Šídák's post hoc test or Kruskal-Wallis test with Dunn's post hoc test was conducted for normal or non-normally distributed data points, respectively. The Benjamini–Hochberg method was used to correct the *p*-values for multiple testing, yielding FDR, where FDR<0.05 was considered as significant. Interpretation of Cliff's δ effect size was according to established cut-offs [43]: negligible ($\delta < 0.15$), small ($\delta \geq 0.15$), medium ($\delta \geq 0.33$), and large ($\delta \geq 0.47$). All analysis was conducted using RStudio, except the boxplot comparison of DE values between different gene sets were conducted using GraphPad Prism v10 (CA, USA).

3. Results

3.1 Identification and characterization of five distinct PCa cell clusters

In the investigated scRNA-seq dataset (GSE185344) [37], two different groups of cases derived from PCa patients were assessed *i.e.*, benign adjacent (NonCa) and PCa groups, each consisting of seven cases. In the NonCa group, *TRPM4* was highly expressed in BP cells (cluster 3; n=890 cells), where its levels were significantly higher in BP than other cell clusters (FDR<0.01) such as immune cells (*e.g.*, NK, NKT, helper T cells, B cells, macrophages), endothelial cells, and fibroblasts (**Figure 1A** and **Supplementary Table 2**).

In the PCa group, UMAP clustering showed that *TRPM4* levels were most elevated, based on median levels, in five distinct PCa clusters *i.e.*, clusters 6 (n=1,869 cells), 9 (n=1,618 cells), 11 (n=1,222 cells), 14 (n=824 cells), and 19 (n=322 cells) (**Figure 1B** and **Supplementary Table 2**). *TRPM4* levels were also elevated, although to a lesser extent, in clusters 16 [potential internal BP (IBP) cells *i.e.*, benign cells found within cancerous cells; n=733 cells] and 22 (epithelial cells; n=38 cells). As *TRPM4* was most highly expressed in cluster 14, *TRPM4* levels in cluster 14 were compared with each of the other cell clusters, showing that *TRPM4* levels were significantly higher in cluster 14 (FDR<0.01) except when compared with cluster 11 or 19.

As the PCa group consisted of seven distinct PCa patients, PCa cell heterogeneity was captured by the UMAP clustering represented as five PCa clusters (clusters 6, 9, 11, 14, and 19), with each cluster positioned adjacent or close to each other in the UMAP plot and with similar *TRPM4* expression levels. Cluster 16 was potentially IBP cells based on its similar *TRPM4* median levels (*TRPM4* log₂: 0.96) with those of BP cells (NonCa group cluster 3; *TRPM4* log₂: 1.02) but lower compared with the aforementioned five PCa clusters (*TRPM4* log₂: all >1.5; **Figure 1B**). To assess this further:

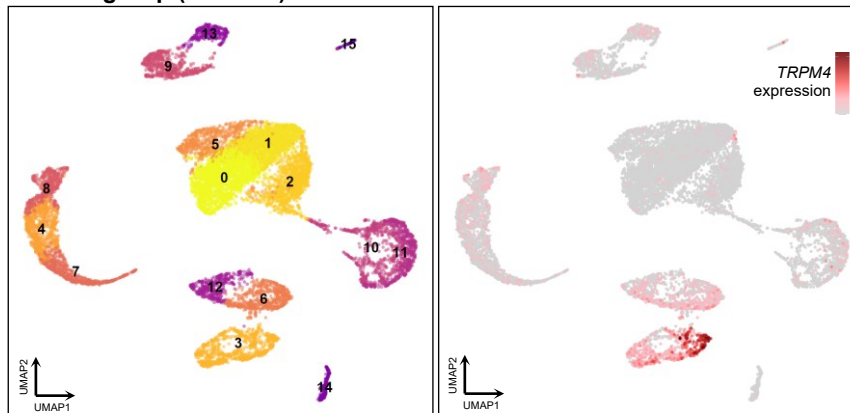
- i) Qualitatively: The top 50 markers representing each cluster (**Supplementary Table 1**) were examined and each of the five PCa clusters demonstrated markers known to be overexpressed in PCa cells *i.e.*, PCa group cluster 6 (*OR51E2*), 9 (*PMEPA1*, *GLIPR1*), 11 (*SCHLAP1*, *CTAG2*), 14 (*NNMT*, *TSPAN8*), and 19 (*PRAC1*). These markers were absent from the top 50 markers significantly associated with the BP cluster (NonCa group cluster 3) or the IBP cluster (PCa group cluster 16). For both BP and IBP clusters, conventional BP markers were present including *MME* and *SCGB1D2*, and these markers were absent from the top 50 markers representing each PCa cluster (clusters 6, 9, 11, 14, and 19).
- ii) Quantitatively: Spearman's r_s and Kendall's τ correlation matrix was constructed to compare the transcriptome profile similarities between BP versus the five PCa and IBP clusters, and epithelial cell cluster (PCa group cluster 22, as controls) (**Figure 1C**). BP and IBP clusters shared high transcriptome similarities ($r_s=0.99$, $\tau=0.91$), while BP cluster showed consistently lower r_s (<0.95) and τ (<0.80) with the rest of the PCa group clusters.

3.2 Spearman–Kendall's dual-filter reveals *TRPM4* correlation with ribosomal gene expression in PCa cells

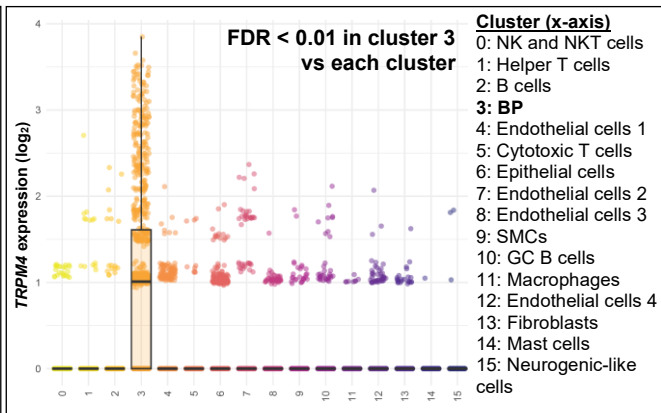
Next, Spearman's r_s and Kendall's τ correlation values of *TRPM4* with all genes in IBP cells (y-axis) and PCa cells from the five PCa clusters (hereby termed as PCa cells for simplicity) were examined, and genes passing the Spearman–Kendall's dual-filter ($r_s > 0.6$ and $\tau > 0.5$)

Figure 1

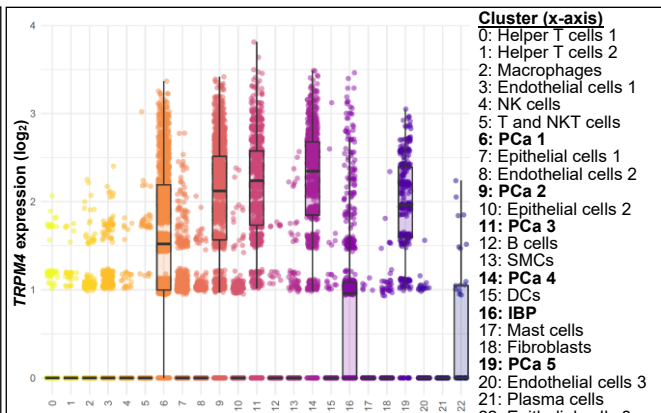
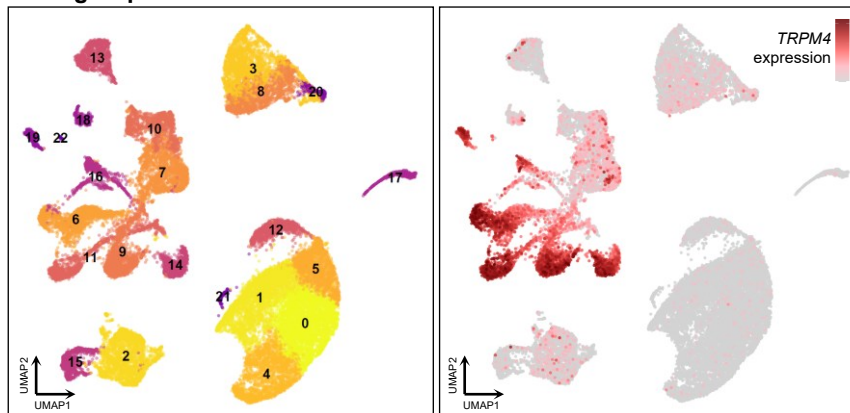
(A) NonCa group (BP cells)



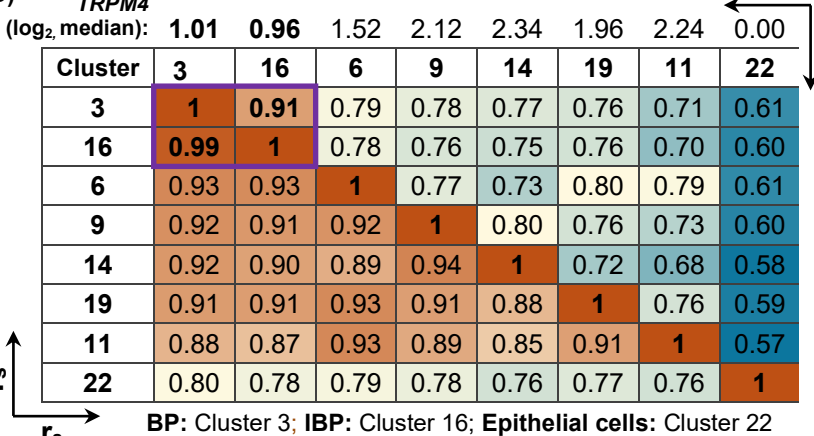
FDR < 0.01 in cluster 3 vs each cluster



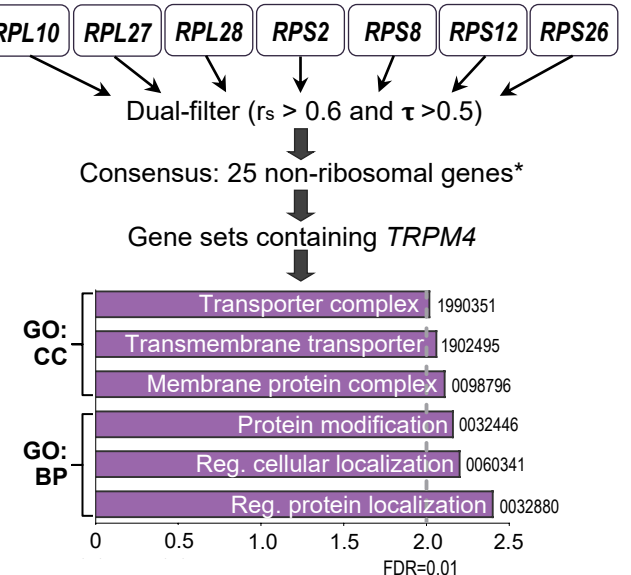
(B) PCa group



(C) TRPM4



(E)



(D)

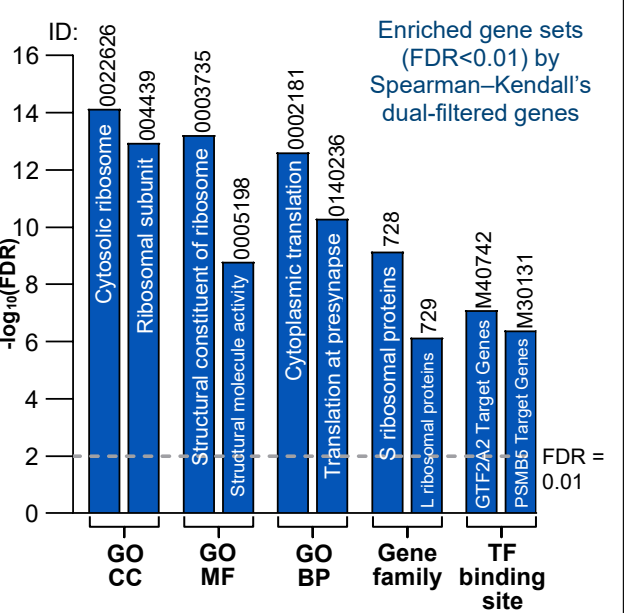
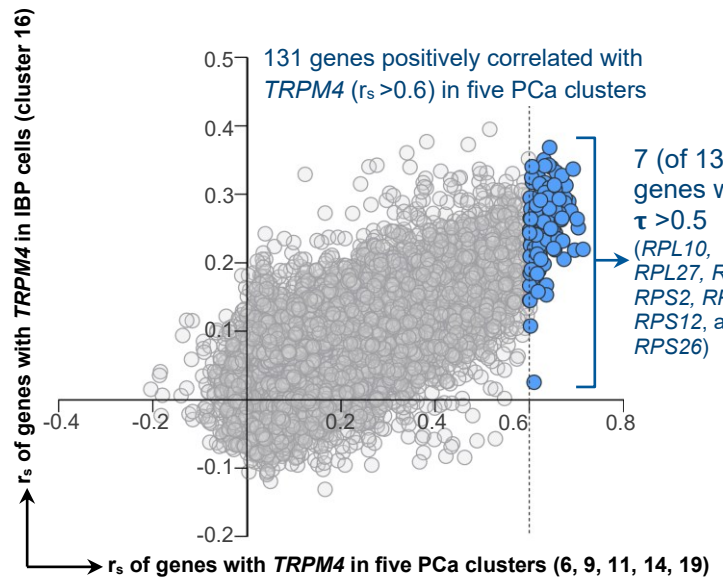


Figure 1. *TRPM4* expression profile and enriched gene sets in scRNA-seq dataset (GSE185344) of PCa and NonCa (n=7 each group). (A) UMAP plot of sixteen cell clusters (0–15) in NonCa group (n=12,205 cells; left panel), *TRPM4* expression levels in the cell clusters (middle panel), and comparison of *TRPM4* expression levels in BP cluster 3 versus each other cluster (right panel); (B) UMAP plot of 23 cell clusters (0–22) in PCa group (n=30,932 cells; left panel), *TRPM4* expression levels in the cell clusters (middle panel), and boxplot with jitter plot comparison of *TRPM4* levels in each cluster (right panel); (C) Spearman r_s and Kendall's τ correlation matrix of BP cluster 3, IBP cluster 16 (from PCa group), and five PCa clusters 6, 9, 11, 14 and 19, and epithelial cells cluster 22. Median levels of *TRPM4* in each cluster are shown on top of the matrix; (D) Scatter plot of r_s values of all genes in relation to *TRPM4* expression in IBP cells (cluster 16 of NonCa group) versus five PCa clusters (clusters 6, 9, 11, 14 and 19). Spearman–Kendall's dual filters were applied to shortlist for *TRPM4*-monotonic genes and the corresponding enriched gene sets (FDR<0.01) shown in bar plot; (E) For each of the seven *TRPM4*-monotonic genes (all ribosomal genes), dual filters were applied to identify consensus genes in the five PCa clusters *i.e.*, the group of genes with r_s >0.6 and τ >0.5 in relation to each of the seven ribosomal genes in PCa cells. A total of 25 non-ribosomal consensus genes were identified and the enriched gene sets (FDR<0.01) containing *TRPM4* are shown in bar plot. *There were 56 ribosomal consensus genes. GO BP: GO Biological Process; GO CC: GO Cellular Component; GO MF: GO Molecular Function; TF: Transcription factor.

were shortlisted (in **Figure 1D**). No gene passed the Spearman–Kendall's dual-filter in IBP cells, but in PCa, seven genes (*RPL10*, *RPL27*, *RPL28*, *RPS2*, *RPS8*, *RPS12*, and *RPS26*) passed the dual-filter (**Figure 1D** and **Supplementary Table 3**). As these seven were ribosomal genes, ribosomal gene sets were significantly enriched (FDR <0.01).

In order to gain preliminary insights on the potential functions of *TRPM4* on those seven ribosomal genes in PCa cells, correlation values (r_s and τ) of all genes with each of the seven ribosomal genes individually were computed, and genes that passed the Spearman–Kendall's dual-filter were shortlisted. For instance, 342 genes showed r_s >0.6 and τ >0.5 (the dual-filter's cut-offs) with *RPL10*, and these genes were considered as *RPL10*-monotonic genes in PCa cells. Subsequently, the dual-filtered genes across each of the seven ribosomal genes were compared for consensus dual-filtered genes, yielding a total of 56 and 25 ribosomal and non-ribosomal genes, respectively. *TRPM4* was one of the 25 non-ribosomal genes that passed the dual-filter for each of the seven ribosomal genes. GO enrichment of the 25 non-ribosomal genes (excluding ribosomal genes to uncover functions regulating or supporting ribosomal processes) was conducted and GOs containing *TRPM4* in their gene lists were shortlisted, demonstrating that regulation of protein or cellular localization, and transporter complex GOs were significantly enriched (FDR<0.01) (**Figure 1E** and **Supplementary Table 4**).

3.3 Validation of gene set representatives and distribution family for GAM analysis

Next, the seven ribosomal genes' expression values were averaged to yield a representative Ribo expression, for each patient separately, for downstream analysis. This excluded the need to model *TRPM4* with each of the seven ribosomal genes separately. Multiple analyses were conducted to test the reliability of averaging the seven ribosomal genes into Ribo as the representative. Cronbach's α (0.969–0.992) and McDonald's ω (0.971–0.991) were >0.95 for all patients, indicating internal consistency of each ribosomal gene expression values across the patients. All patients' KMO values were >0.90 (0.934–0.961), supporting sampling adequacy for downstream factor analysis utilizing Ribo. The CS score (average of Cronbach's α , McDonald's ω , and KMO scores) for averaging into Ribo was >0.95 and >0.85 in PCa and BP cells, respectively (**Supplementary Table 5**).

AR signaling is a key pathway that controls prostate-specific gene expression in both BP and PCa cells [44], and *TRPM4* is expressed in androgen-sensitive PCa cells potentially involved

in their AR signaling [18, 45]. Hence, seven common AR pathway genes were included (*i.e.*, *ABHD2*, *ALDH1A3*, *KLK2*, *KLK3*, *KLK4*, *PDLIM5*, and *SORD*) and averaging them to represent AR as a control group to compare with Ribo in downstream modeling. The CS for averaging into AR was >0.85 (except Pt.5 CS of 0.814) and >0.74 (except Pt.5 CS of 0.663) in PCa and BP cells, respectively (**Supplementary Table 5**). Heatmap of each of the seven ribosomal and AR pathway genes, and their averaged representatives Ribo and AR, in PCa and BP cells are presented in **Figure 2**.

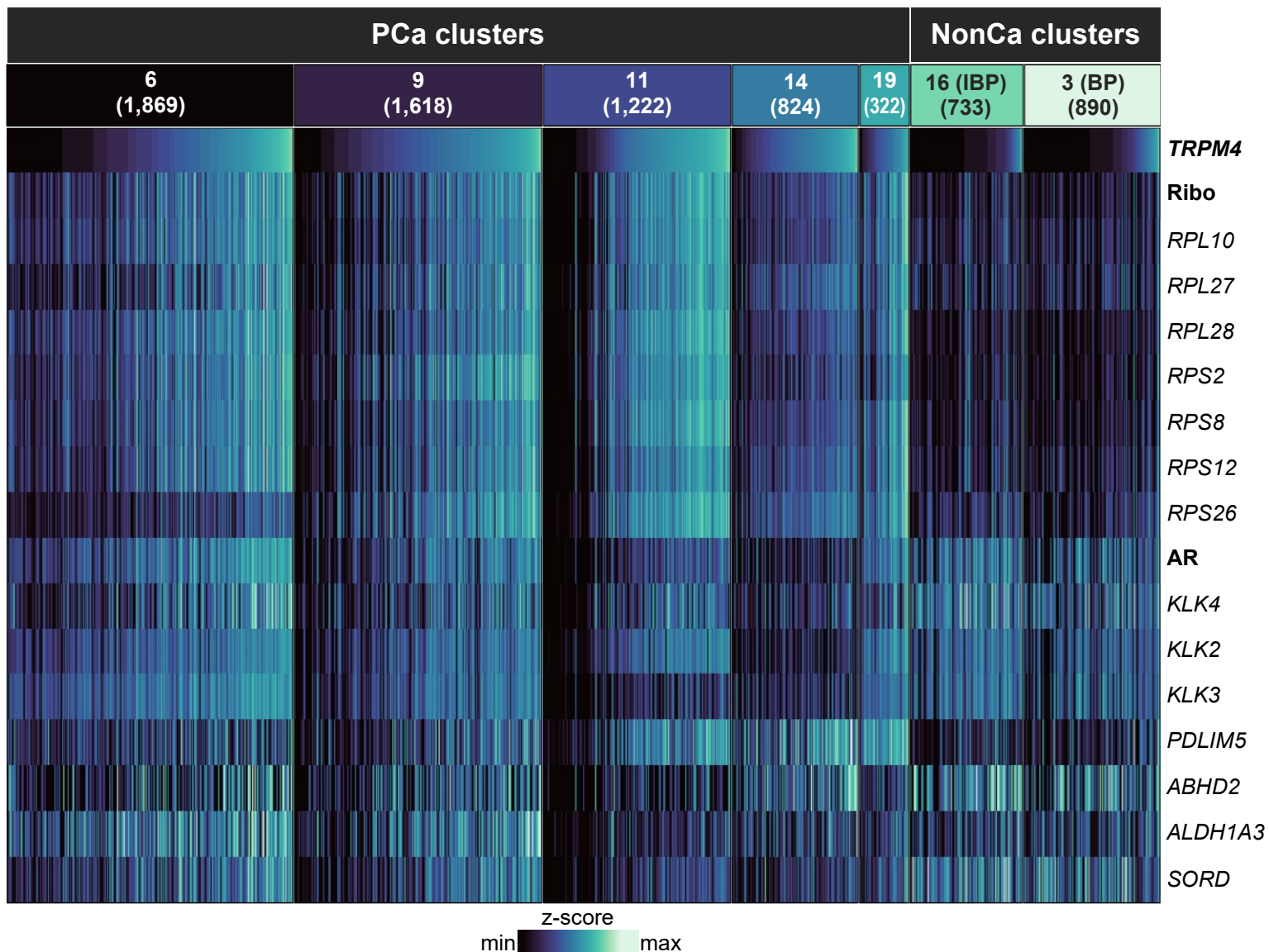


Figure 2. Heatmap visualization of mean ribosomal genes' expression (Ribo), mean AR signaling expression, individual ribosomal and AR signaling genes in PCa and NonCa clusters. The cells were ordered according to ascending *TRPM4* expression in each cluster. Number of cells within each cluster are shown in brackets.

As the gene expression data had been pre-processed by removing cells with zero gene expression, subsequently log₂-transformed, while Ribo and AR were aggregates (*i.e.*, average expression of seven genes each), the data distribution may have been transformed to a more continuous and less skewed pattern, approximating a Gaussian distribution. Hence, the `gam.check()` standard diagnostic plots were generated to qualitatively assess the suitability of model fitting with Gaussian GAM.

For *TRPM4*-Ribo and *TRPM4*-AR modeling in PCa cells (the main models in this study), Q-Q plots showed that residuals aligned closely with the diagonal line (*i.e.*, normal distribution) although with deviations at both ends of the data, while the histogram of deviance residual plots demonstrated bell-shaped distribution centered around zero (**Supplementary Figure 1**). The deviance residuals versus fitted values plot, and response versus fitted values plot qualitatively suggested homoscedasticity and sufficient model fitting, respectively.

To validate these observations using independent metrics, the Akaike information criterion (AIC), Bayesian information criterion (BIC), and DE were computed after GAM fitting with Gaussian, negative binomial, gamma, inverse Gaussian, and quasi-Poisson family of distributions. Gaussian GAM yielded the lowest AIC and BIC, and the highest DE, across all modeling (except for Pt.4 *TRPM4*-AR modeling in BP cells where all families tied with the same DE) compared with the other distribution families (**Supplementary Table 6**). Thus, Gaussian GAM was utilized for modeling in this study.

3.4 Convergence and explainability of REML and PRSS in *TRPM4*-Ribo modeling

As explainability is vital for the implementation and optimization of any ML model, particularly in medical AI applications where model decisions should be explainable for clinical translation, the overall workflow and mechanism of GAM in this study are presented in **Figure 3**. The main objective was to determine how much *TRPM4* expression can explain the variability in Ribo expression based on GAM, with minimal overfitting or underfitting. The initial GAM model was specified to contain linear terms (intercept and a linear term) and smooth terms (with multiple smooth basis functions), with each term containing its own coefficient (magnitude of their effects) determined and optimized by REML and PRSS (**Figure 3**).

For each PRSS iteration, optimization of the smoothing parameter λ was performed according to REML, where REML iterated until convergence according to the Newton–Raphson method. Across 98 GAM models [7 samples \times 7 gene sets \times 2 cell types (PCa and BP)], gradient-based convergence (60/98 instances) was the most common form of REML convergence, followed by score-based convergence (37/98 instances), fallback convergence (1/98 instances occurring in Pt.7 *TRPM4*-PI3K/AKT modeling in BP cells), and none with maximum number of iterations reached (**Supplementary Table 7**).

The REML iteration with the lowest REML score was selected by the algorithm as the best model, and this selected REML iteration provided the optimized λ . Hence, each PRSS conducted its own λ optimization by minimizing REML (the inner loop *i.e.*, REML nested within PRSS), and the resulting best λ was then used to determine PRSS value (the outer loop). The earliest PRSS iteration with the lowest PRSS value was selected as the final model (extended descriptions and example results of REML and PRSS iterations are presented in the next Results subsection). The REML-optimized λ was used to penalize the splines (*i.e.*, TPRS basis functions) in PRSS, where the product of λ and integral of the squared second derivative $f''(x)$ (the curvature) represents the penalized spline. More curvature leads to higher integral value, and the curvature is penalized by λ to avoid overfitting (*i.e.*, fitted GAM curve that is jagged or “chases” every data point), resulting in a smoother GAM curve as exemplified in **Figure 3** (section III).

In terms of GAM performance metrics, the DE in percentage was adopted to quantify how much of Ribo expression variability was captured by *TRPM4* expression (**Figure 3**, section IV). To identify individual cells with strong *TRPM4*-Ribo relationship, CEP classification of the cells into TREP and non-TREP cells were conducted based on individual cell's EP value and ranking. These cells were subsequently binarized into TREP or non-TREP cells based on the overall modeling DE%, before the biology of TREP and non-TREP cells were investigated (**Figure 3**, section V).

Figure 3

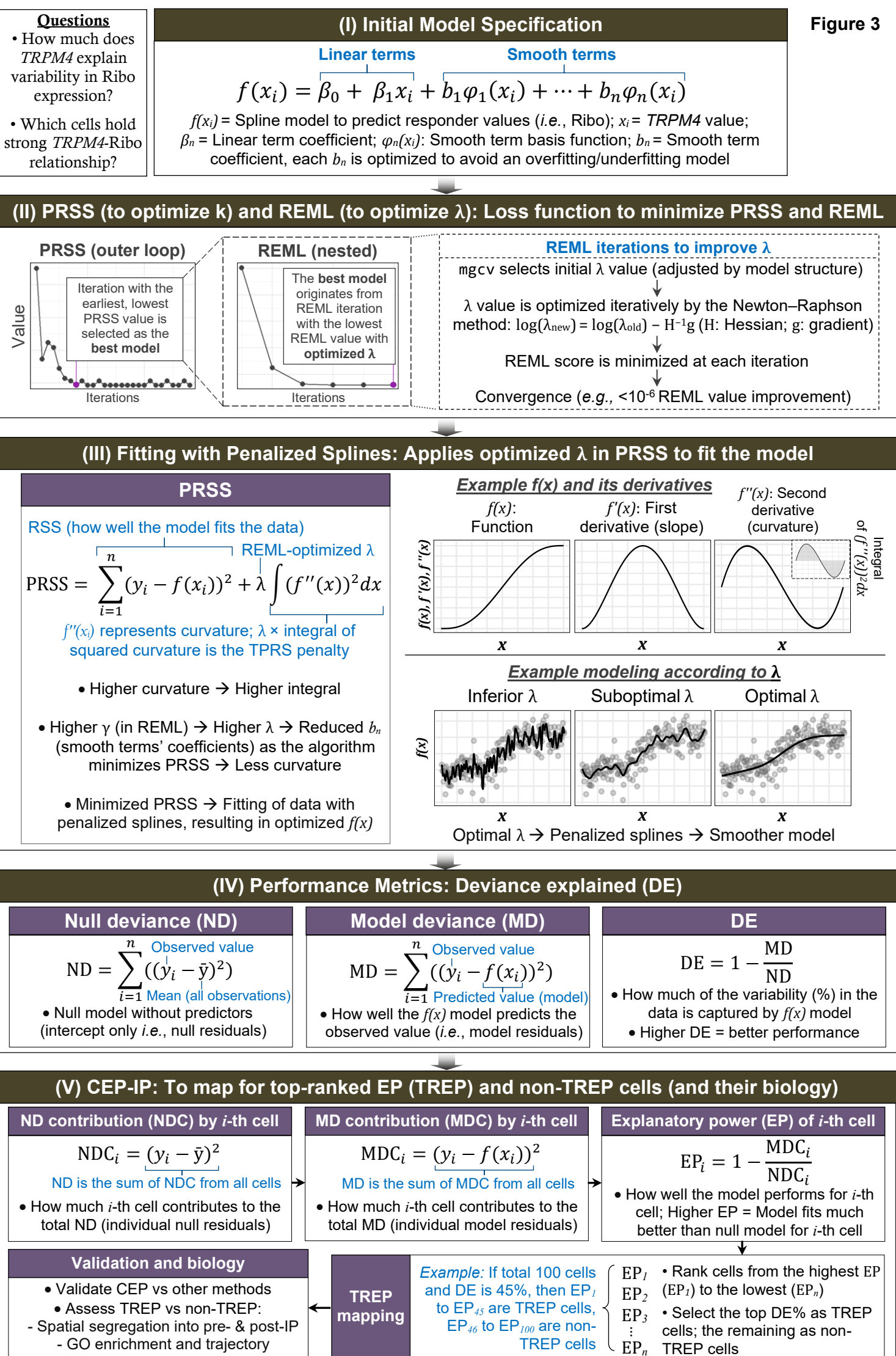


Figure 3. Workflow of Gaussian GAM in this study. The study was initiated by specifying the function with linear and smooth terms. Next, REML optimization was conducted to obtain the optimal λ value. Each PRSS iteration minimized REML score until convergence, and PRSS was treated as a hyperparameter space for optimization with different k values. The best model (with the optimal k and λ) was determined by the earliest, lowest PRSS value. In the PRSS step, each spline term was penalized by the REML-optimized λ (i.e., TPRS penalty), leading to a smoother GAM fit. The optimized model with penalized splines was then selected to calculate DE (i.e., how much *TRPM4* expression can capture the variability in Ribo expression). CEP classification was performed where EP values of each individual cell were ranked from the highest to the lowest, and the top DE% were selected as TREP cells. Validation of the cell classification methodology, and biology of the classified cells were subsequently investigated. By preserving transparency in both model optimization and cell-level predictions, this workflow enables biological interpretation of ML outputs and serves as an example of XAI modeling.

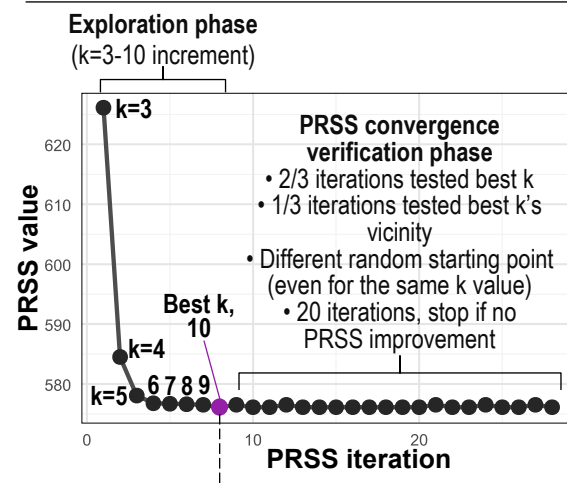
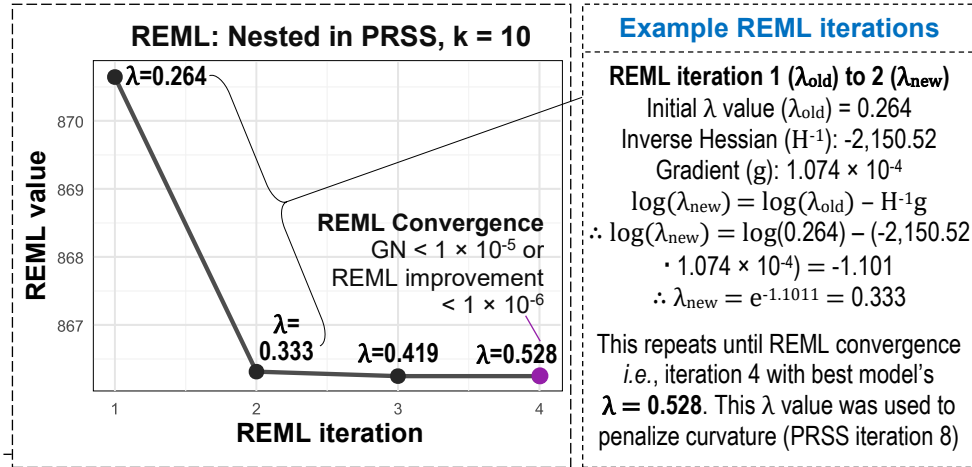
Optimal GAM curvature penalization, without being overly restrictive (underfitting) or permissive (overfitting) in the penalization, was finetuned by minimizing REML (inner loop) and PRSS (outer loop) until convergence. To illustrate this more clearly, *TRPM4*-Ribo modeling in Pt.4 was demonstrated as an example in **Figure 4A**. For each PRSS iteration, REML iterations until REML convergence occurred to obtain the best REML score (i.e., lowest REML score, as the loss function of the algorithm was to minimize REML), and precise calculations of REML iteration 1 ($\lambda=0.264$) to iteration 2 ($\lambda=0.333$) according to Newton–Raphson method operating on gradient and inverse Hessian values are illustrated in **Figure 4A**. Upon REML convergence, that specific REML iteration yielded the best REML, along with its optimized λ value that was subsequently used to penalize GAM curvature (PRSS iteration 8 in this example).

In PRSS (the outer loop), it consisted of two phases: (i) Exploration phase testing $k=3–10$ in increment (k denotes the maximum number of spline basis functions, φ , for GAM modeling); (ii) Convergence verification phase that tested 20 additional iterations with different k values, where a third of the iterations tested best k value obtained from the exploration phase and the rest of the iterations tested best k 's vicinity. PRSS convergence was considered when there was no further improvement in its value and all modeled relationships' PRSS converged within this phase. As the loss function was to minimize PRSS value, the earliest iteration that yielded the lowest PRSS value was selected as the final, best model. This PRSS iteration contained its REML-optimized λ used to penalize the spline basis functions. The consolidated REML and PRSS results (e.g., k , λ , REML and PRSS values) for all iterations and multiple gene sets investigated (e.g., Ribo, AR) in PCa or BP cells separately, and each of their best model's REML iteration parameters (gradient and Hessian) are presented in **Supplementary Table 7**.

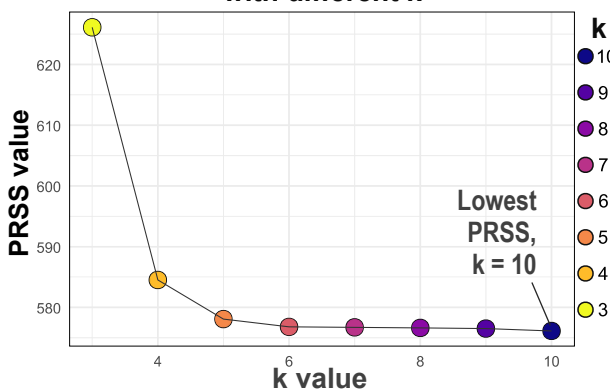
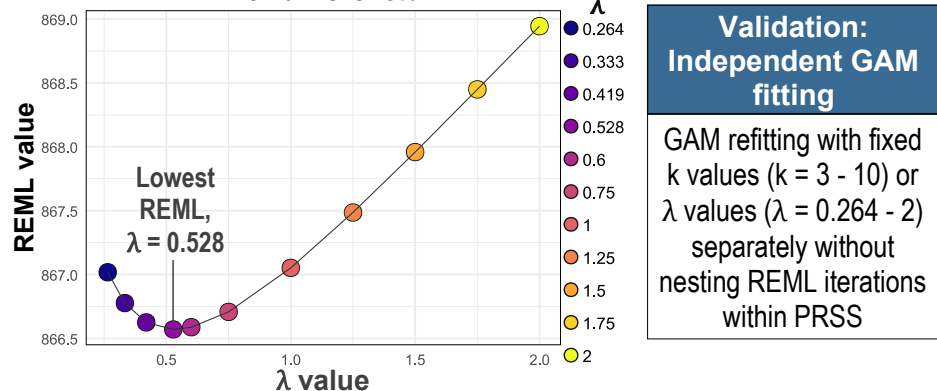
To test if the best model chosen by the converged PRSS and REML was valid, an independent GAM fitting without nesting REML within PRSS (i.e., without the outer and inner loops structure found in the original PRSS and REML optimization workflow) was performed using fixed k values ($k=3–10$) and λ values derived from the original optimization (Pt.4: $\lambda=0.264$, 0.333, 0.419, and 0.528) with additional λ values beyond the original best model's λ (e.g., $\lambda=0.6$, 0.75, 1, 1.25, 1.5, 1.75, and 2). The aim was to observe if this independent GAM fitting with fixed k values and wider range of λ values resulted in the same best k and best λ values with the original REML and PRSS optimization process. As shown for *TRPM4*-Ribo modeling in Pt.4, the independent GAM fitting with fixed k and λ values showed that the lowest PRSS and REML scores yielded $k=10$ and $\lambda=0.528$, respectively, aligning with the best k and best λ values derived from the original GAM fitting (**Figure 4B**).

In the rest of the patients, the independent *TRPM4*-Ribo GAM fitting also resulted in best k and best λ that tallied with the original REML and PRSS optimization, except Pt.6 where the independent GAM fitting yielded different best λ (original best $\lambda=5099.360$ vs. independent best $\lambda=9000$). However, the REML scores for these two distinct GAM fittings differed by <0.001 (rounded up to 0.0002; **Supplementary Table 7**), where both of their REML scores were 1,229.607 (**Figure 4C**), suggesting that a huge range of λ values may be within a flat region of REML optimization surface where the objective function was insensitive to λ changes. Monotonic decrease in REML value of <0.001 for each successive iteration was observed, thus REML minimization still occurred but with diminishing returns in further λ optimization.

(A)

PRSS: Outer Loop**Figure 4**

(B)

PRSS: Independent GAM fitting with different k **REML: Independent GAM fitting with different λ** 

(C)

PCA (Ribo gene set)	PRSS: Best k	REML (nested in PRSS): Best λ	Independent GAM fitting	
			Best k	Best λ
Pt.1	6	1.570	6	1.570
Pt.2	3	0.079	3	0.079
Pt.3	6	0.139	6	0.139
Pt.4	10	0.528	10	0.528
Pt.5	4	0.287	4	0.287
Pt.6	4	5099.360	4	9000
Pt.7	3	1.287	3	1.287

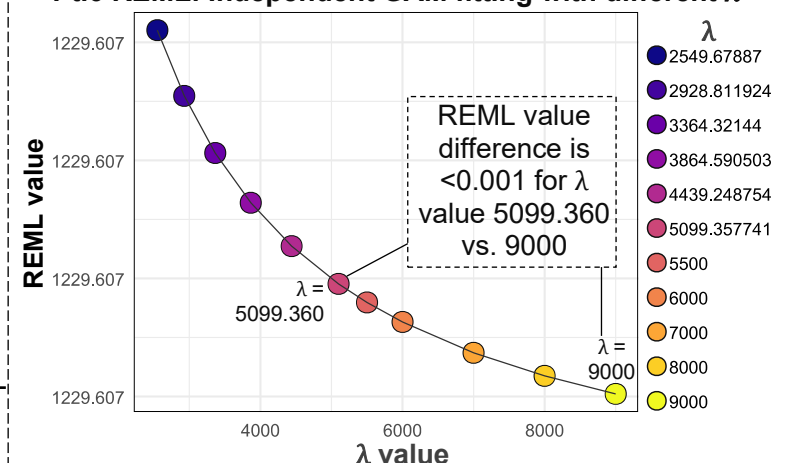
Pt.6 REML: Independent GAM fitting with different λ 

Figure 4. PRSS and REML iterations of *TRPM4*-Ribo modeling represented by PCa cells in Pt.4 as the representative, and validation of PRSS and REML best models. (A) PRSS consisted of 28 iterations, divided into exploration phase (testing $k=3-10$ increment) and PRSS convergence verification phase (additional 20 iterations and stopped if no further reduction in PRSS). Each PRSS iteration minimized REML via the Newton-Rhpson method until REML convergence as defined by $GN < 1 \times 10^{-5}$ or REML improvement $< 1 \times 10^{-6}$. The inverse Hessian value was backcalculated using λ_{old} , λ_{new} , and gradient value (**Supplementary Table 7**); (B) GAM refitting with fixed k values (3–10) optimized by PRSS (left panel), or with different λ values (0.264–2) optimized by REML (right panel); (C) Best model's PRSS, REML, k , and λ values for each patient, and Pt.6 was highlighted showing minimal difference (< 0.001) in REML value when fitted using λ value (5099.360) optimized by REML nested in PRSS method versus a fixed λ value (9000).

3.5 Explainable spline penalization and formation of the full *TRPM4*-Ribo model

For further explainability, a schematic representation of GAM splines formation in *TRPM4*-Ribo modeling (Pt.4) with mgcv is demonstrated in **Figure 5A**. Initially, basic statistical assessment was performed on the data (e.g., mean, range) to guide the construction of representative knots (dotted lines) (**Figure 5A**). The splines (TPRS basis functions) were then initialized surrounding the knots, and in this case there were eight splines (φ_1 to φ_8) determined by the best k value ($k=10$ basis functions total, with φ_1 to φ_8 representing the eight main splines shown here, while φ_9 to φ_{10} had been penalized out of the final model).

The splines were subsequently processed based on the data distribution and data density at knots, forming unweighted and unpenalized splines in their raw form with obvious curvatures, particularly φ_3 to φ_7 . The coefficient of each spline was estimated by REML, with the λ value controlling the penalty strength and applied in PRSS to weight and penalize each spline, reducing their curvature and minimizing overfitting. Coefficient values below $|1.0|$ resulted in reduced curvature or magnitude of the individual spline, while negative coefficient value caused the individual spline's direction to invert.

Next, the weighted and penalized splines were combined to collectively form a smooth curve (representing the smooth terms), and the combination of linear terms with smooth terms formed the final full GAM model, where *TRPM4* values as the predictor of Ribo values for each cell such as Cell #1 [linear terms + smooth terms = $5.15 + (-1.92) = 3.23$, representing the predicted Ribo value given the actual *TRPM4* value of Cell #1] (**Figure 5A**). The variance contribution of each linear and smooth terms was also computed, and φ_1 showed the largest contribution (49.7%) (**Figure 5B**), aligning with the shape of the penalized and weighted collective smooth curve that reflects the characteristic sigmoidal shape of penalized and weighted φ_1 individual spline.

3.6 Final model optimization through γ parameter tuning and visual assessment

Higher REML's γ value typically leads to higher λ value, resulting in more penalization on spline's curvature. Hence, splines smoothing to yield the optimal GAM curves, avoiding overfitting or underfitting, can be achieved by adjusting for the ideal γ value. To this end, *TRPM4*-Ribo or *TRPM4*-AR modeling was conducted for PCa, BP, and IBP cells in all patients (Pt.1–Pt.7) using mgcv default $\gamma=1$, and to observe overfitting (fluctuating) or underfitting (overly smooth) characteristics in the resulting GAM curves.

Figure 5

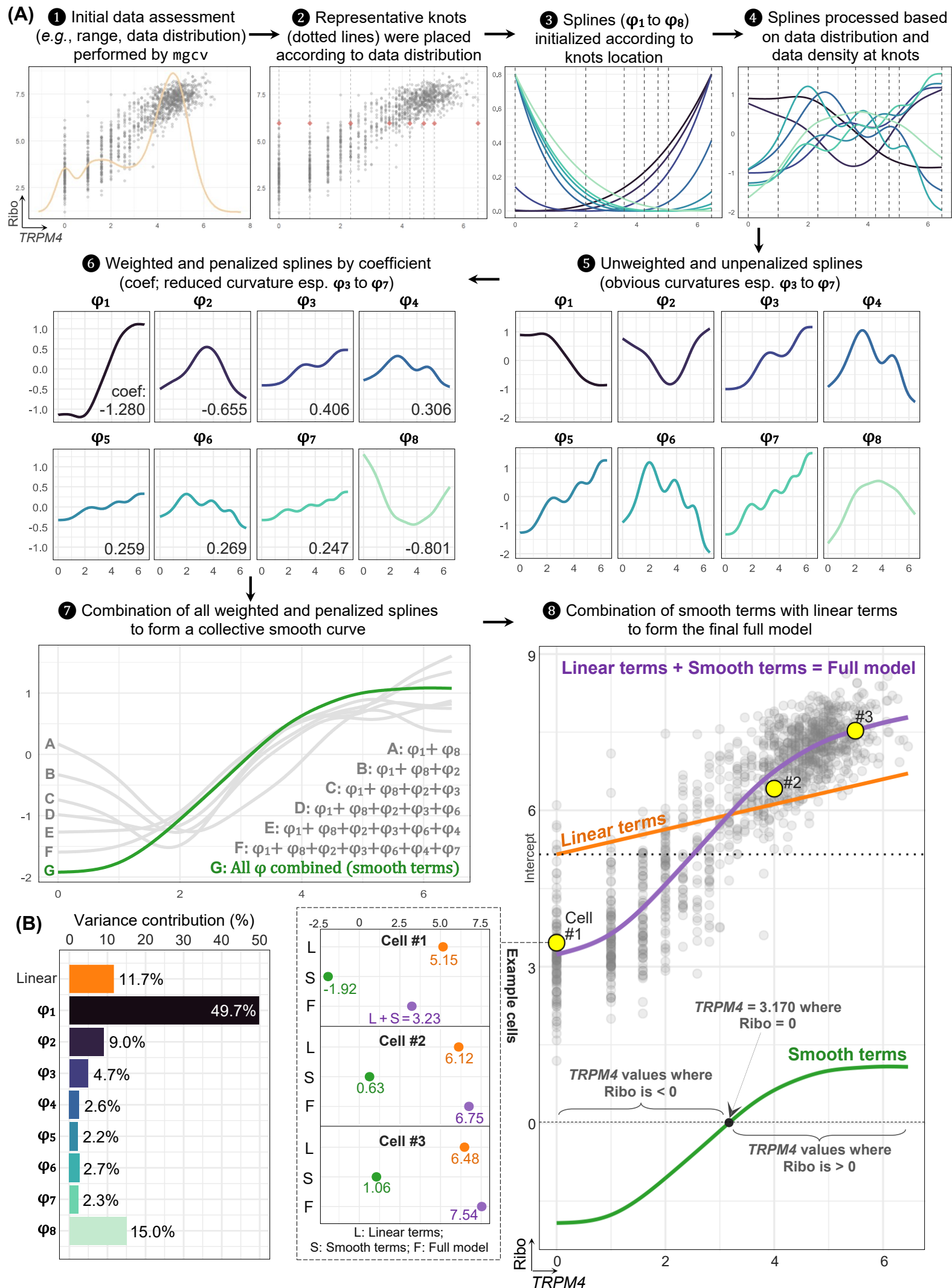


Figure 5. Visualization of GAM's TPRS formation represented by Pt.4 *TRPM4*-Ribo modeling. (A) Schematic representation of the formation of the TRPS basis functions and final full model. Number of splines was determined by the best model's k value, and each was penalized by REML-optimized λ as reflected by each spline's coefficient. Combination of linear and smooth terms formed the final full model, and three representative cells (Cell #1, #2, and #3) were selected as examples illustrating that combination of linear and smooth terms' Ribo values, yielding the full model's predicted Ribo value; (B) Variance contribution of linear and each spline (φ_1 to φ_8) terms to the full model.

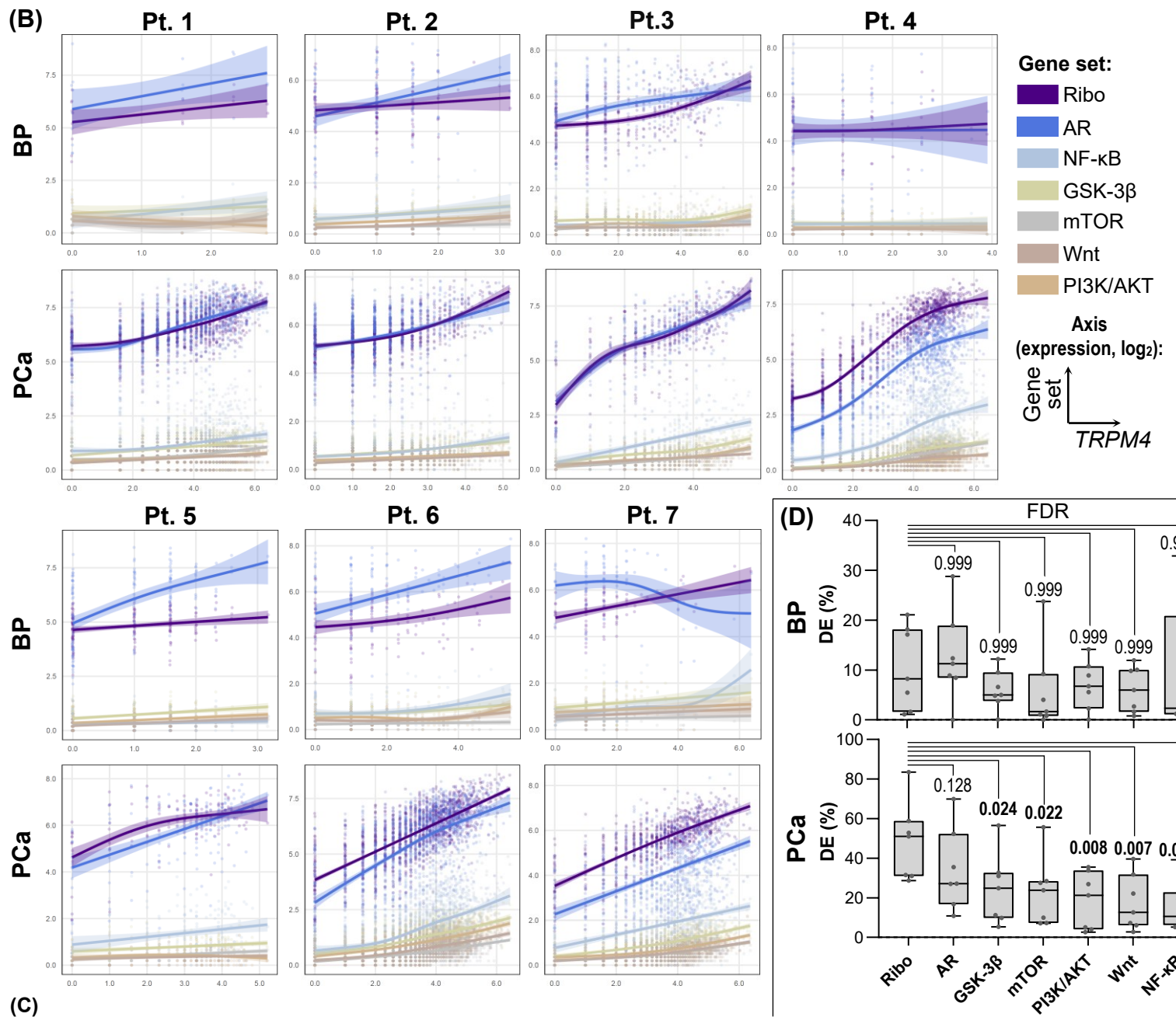
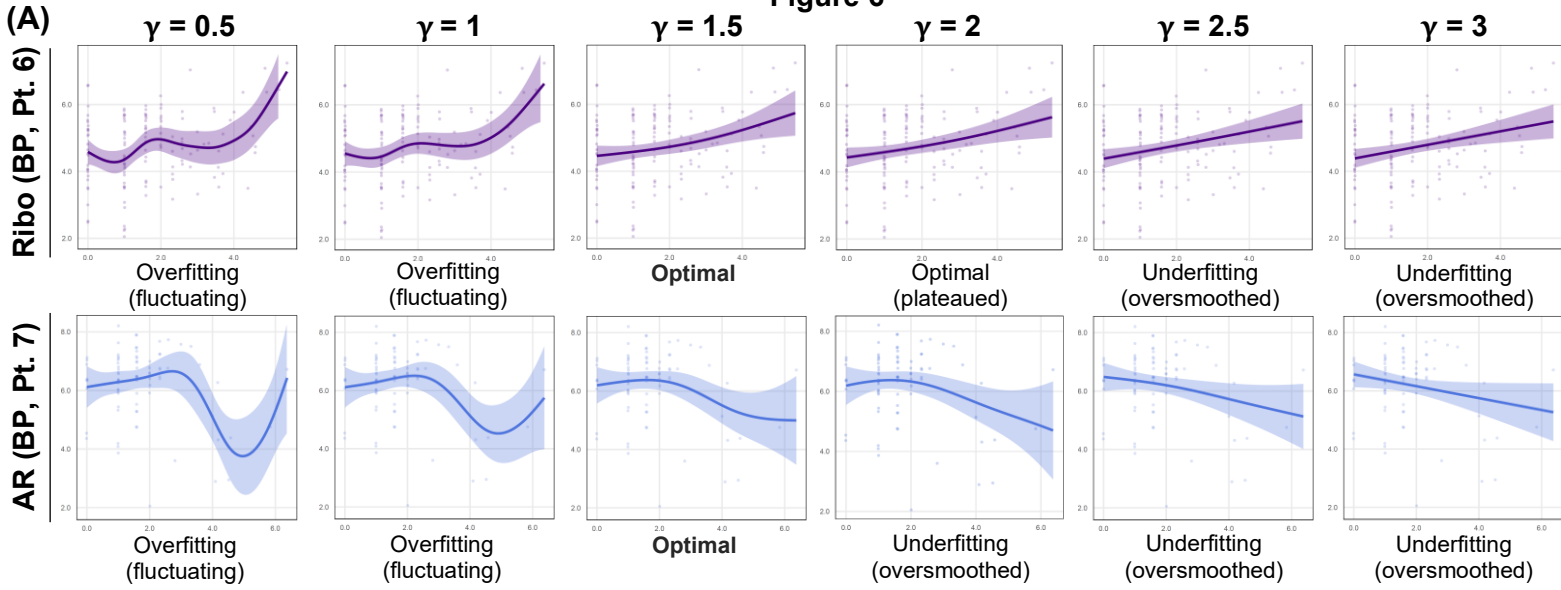
In PCa cells, all the patients showed relatively stable *TRPM4*-Ribo and *TRPM4*-AR GAM curves without obvious signs of overfitting or underfitting. However, in BP cells, Pt.6 (*TRPM4*-Ribo) and Pt.7 (*TRPM4*-AR) GAM curves showed overfitting characteristics with fluctuations (**Supplementary Figure 2**). In IBP cells, *TRPM4*-AR also exhibited signs of overfitting in Pt.1 and Pt.3, but four of the patients, Pt.2, Pt.4, Pt.5, and Pt.7, did not have sufficient IBP cells for the modeling. In view of this, PCa and BP cells were subsequently prioritized for downstream optimization by attempting multiple different γ values in 0.5 increment (*i.e.*, $\gamma=0.5, 1, 1.5, 2, 2.5$, and 3) in order to improve the characteristics of the GAM curves via visual inspection. Assessment with the range of γ values showed that $\gamma=1.5$ yielded optimal smoothing for *TRPM4*-Ribo (Pt.6) and *TRPM4*-AR (Pt.7) GAM curves of BP cells, mitigating the overfitting characteristics observed previously with $\gamma=1$ (**Figure 6A**). Hence, $\gamma=1.5$ was adopted for all subsequent GAM modeling for comparable results between different models. The optimization results and statistical performance metrics (*e.g.*, DE, model equation) utilizing different γ values are presented in **Supplementary Table 8**.

3.7 *TRPM4*-Ribo outperforms alternative cancer pathways in PCa

Modeling of *TRPM4* with Ribo and AR, as well as with other pathways reported to involve *TRPM4* in cancers including GSK-3 β [46], mTOR [47], NF- κ B [13], PI3K/AKT [47, 48], and Wnt [19] (gene sets averaged from seven typical genes implicated in each pathway; **Supplementary Table 9**), were conducted with $\gamma=1.5$. The resulting GAM curves of *TRPM4*-Ribo and *TRPM4*-AR showed higher gene set expression values (y-axis) than the rest of the gene sets investigated in PCa or BP cells (**Figure 6B**).

Additionally, *TRPM4*-Ribo and *TRPM4*-AR GAM curves demonstrated similar shape in PCa cells across all patients (except Pt.5), such as sigmoidal shape in Pt.4. For explainability and transparency, the calculation of the model's predicted Ribo expression (*i.e.*, prediction made by *TRPM4*-Ribo modeling) for a single PCa cell, with known Ribo ($y_1=7.529$) and *TRPM4* ($x_1=5.492$) expression values, was illustrated in **Figure 6C**. The predicted Ribo expression value was the sum of two linear terms and eight smooth terms (weighted and penalized by their coefficient). DE (83.46%) of the *TRPM4*-Ribo modeling in Pt.4 was calculated as the performance metrics of how much variability in Ribo expression was captured by *TRPM4*. Comparison of *TRPM4*-Ribo DE with other modeled gene sets (AR, GSK-3 β , mTOR, NF- κ B, PI3K/AKT, and Wnt) in BP cells (**Figure 6D**) or IBP cells (**Supplementary Figure 3**) showed that none demonstrated significant difference, but in PCa cells *TRPM4*-Ribo DE was significantly higher than other modeled gene sets (GSK-3 β , mTOR, NF- κ B, PI3K/AKT, and Wnt; all FDR <0.05) except with *TRPM4*-AR DE (FDR=0.128; **Figure 6D**). The complete set of performance metrics, observed and model-predicted values, and smooth basis functions' coefficients of *TRPM4* modeling with all investigated gene sets in PCa cells ($\gamma=1.5$) are presented in **Supplementary Table 9**. These results verified the suitability of *TRPM4*-Ribo relationships for CEP-IP framework modeling to identify therapeutically meaningful signatures.

Figure 6

**(C)**

Pt.4 TRPM4-Ribo model in PCA (example DE calculation)

Model function, $f(x_i) = 5.155 + 0.241x_i + (-1.280)\varphi_1(x_i) + (-0.655)\varphi_2(x_i) + 0.406\varphi_3(x_i) + 0.306\varphi_4(x_i) + 0.259\varphi_5(x_i) + 0.269\varphi_6(x_i) + 0.247\varphi_7(x_i) + (-0.801)\varphi_8(x_i)$

→ ∴ **Model's Ribo expression value,** $f(x_1) = 7.535$ (Actual observed value, $y_1 = 7.529$)

For the first cell, $x_1 = 5.492$; $\varphi_1(x_1) = -0.836$; $\varphi_2(x_1) = 0.703$; $\varphi_3(x_1) = 0.923$; $\varphi_4(x_1) = -0.587$; $\varphi_5(x_1) = 0.780$; $\varphi_6(x_1) = -0.564$; $\varphi_7(x_1) = 0.795$; $\varphi_8(x_1) = -0.006$

$x_i = TRPM4$ value for each cell; $\varphi_i(x_i) =$ Basis function value

PCA cells in Pt. 4: $n=1,232$ (each with own TRPM4 value)

Calculate $f(x_i)$ for all 1,232 cells. Then, compute $\sum(y_i - f(x_i))^2$ as the model deviance.

Null deviance (ND) = 3,465.582;

Model deviance (MD) = 573.051

∴ **Deviance explained (DE) = 83.46%**

Figure 6. GAM modeling in BP and PCa cells. (A) Six different gamma values ($\gamma=0.5-3$) were tested for *TRPM4*-Ribo (Pt. 6 adopted as the reference) and *TRPM4*-AR (Pt. 7 adopted as the reference) in BP cells, where balanced smoothing was observed utilizing $\gamma=1.5$ in the fitting process; (B) GAM modeling in BP (top graphs) and PCa (bottom graphs) cells in each of the seven patients for Ribo, AR, GSK-3 β , mTOR, NF- κ B, PI3K/AKT, and Wnt gene sets; (C) Example DE calculation from *TRPM4*-Ribo modeling in Pt.4 PCa cells. Up to three decimal points were used in this calculation for simplicity, and the original values of the basis functions (**Supplementary Table 9**) contain values up to 15 decimal points; (D) DE comparison of *TRPM4*-Ribo versus *TRPM4* modeling with other gene sets in BP and PCa cells, and FDR <0.05 is in bold.

3.8 CEP classification validation: CEP-classified TREP cells are well-predicted by GAM's DE

As GAM's DE indicated how much variability in Ribo expression can be captured by *TRPM4* expression, the next question to address was which individual cells were most well-predicted by the fitted model, and these cells may be biologically distinct from the remaining cells. GAM's DE was a metric aggregated from all cells, in which ND and MD were the sum of all cells' null and model residuals, respectively. To decompose this aggregate measure into cell-level, individual cell's NDC, MDC, and EP were computed. Each cell was then ranked from the highest to the lowest according to their EP values, and the top DE% of cells were selected and classified as TREP cells (**Supplementary Table 10**). For comparison with the CEP classification of cells into TREP or non-TREP, cells were instead randomly classified or through the leverage-based classification, where their GAM plots showed dissimilar pattern of TREP and non-TREP cells distribution (**Figure 7A**).

MCCV (train:test split of 70:30 for 20 randomized iterations) showed that random or leverage-based classification did not yield significant difference in RMSE of their assigned TREP or non-TREP cells in the test set (**Figures 7B and 7C**). Essentially, CEP-classified TREP cells showed significantly lower RMSE than non-TREP cells across all seven PCa patients in the test set (FDR <0.001 ; **Figure 7D** and **Supplementary Table 11**). For explainability and transparency, example calculation of a CEP-classified TREP cell's EP value is shown in **Figure 7E**.

Figure 7

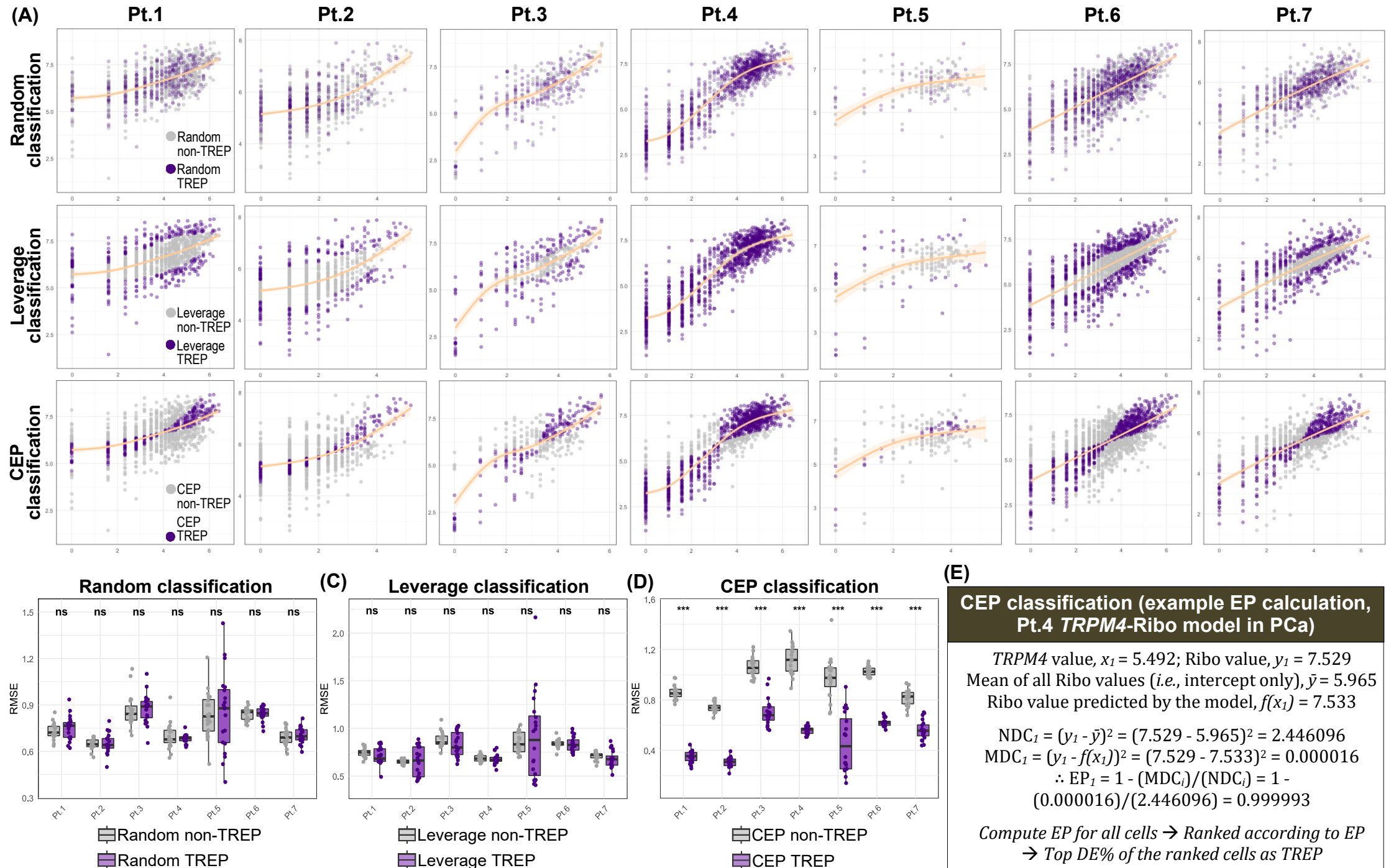


Figure 7. GAM plot distribution patterns and MCCV of TREP and non-TREP cells classified by random, leverage, or CEP classification. (A) Distribution patterns of TREP and non-TREP cells based on the three classification systems; (B-D) MCCV of the performance of random (B), leverage (C), or CEP (D) classification, where lower RMSE in test set's TREP compared with non-TREP group indicated better performance. ***: FDR<0.001; ns: not significant FDR; (E) Example calculation of EP value of a CEP-classified TREP cell, given the actual observations (x_1 and y_1), mean (\bar{y}) and $f(x_1)$ model-predicted Ribo values, to compute NDC₁, MDC₁, and EP₁.

3.9 CEP-classified TREP cells exhibit preference for consistent *TRPM4* and Ribo expression states in pre-IP and post-IP regions

Implementation of the complete CEP-IP framework required combining CEP classification with IP analysis to create distinct cell subpopulations. In *TRPM4*-Ribo modeling, although the DE from all PCa patients were significantly higher than other gene sets (except AR), a wide range of DE was captured across the patients ranging from the lowest 28.6% (Pt.2) to the highest 83.5% (Pt.4), with median DE of 51.1% (**Figure 8**). In order to explain why certain patients showed low or high DE in the *TRPM4*-Ribo modeling, the following key concepts were first investigated:

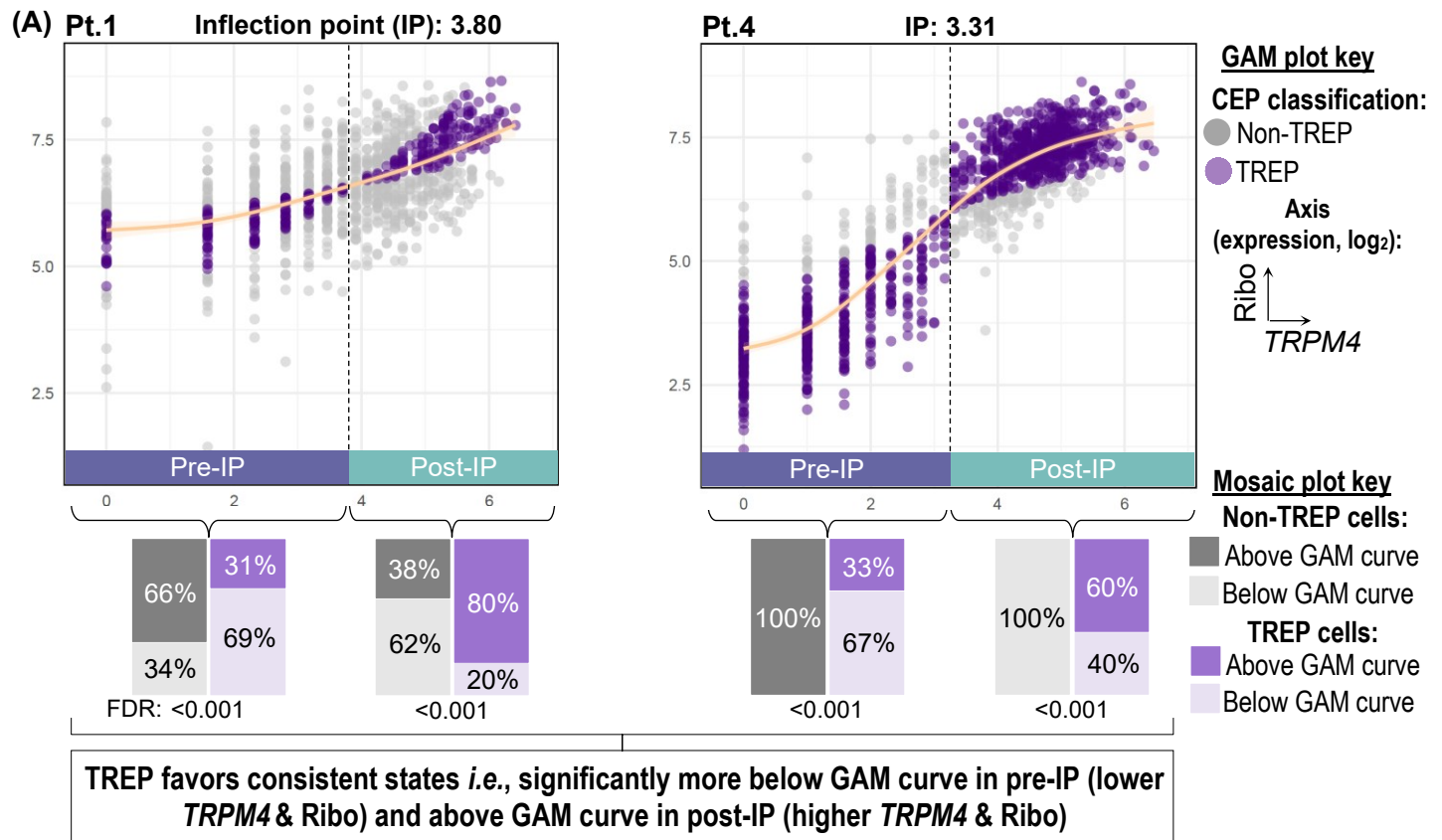
- i) CEP classification of TREP and non-TREP cells.
- ii) Visualizing the distribution pattern of TREP (colored in purple) and non-TREP (colored in gray) cells in scatter plots with the fitted GAM curve.
- iii) Determining the IP *i.e.*, the point on the x-axis (*TRPM4* value) where the distribution pattern of TREP and non-TREP cells shifted, and this was obvious visually only when concepts #1 and #2 above had been implemented.

Based on the aforementioned concepts, it was observed that TREP cells were more frequently found below the GAM curve before the IP (pre-IP *i.e.*, the region with lower *TRPM4* levels), and this pattern was inverted after the IP (post-IP *i.e.*, the region with higher *TRPM4* levels) where more TREP cells were found above the GAM curve, as exemplified by Pt.1 and Pt.4 in **Figure 8A** (FDR<0.001 for all proportion comparison shown in mosaic plots). In contrast, non-TREP cells were more frequently found above or below the GAM curve in pre-IP or post-IP, respectively. This distribution pattern was more obvious in Pt.4, with a sigmoidal GAM curve, where 100% of non-TREP cells were found above or below the pre-IP or post-IP region, respectively (FDR<0.001; **Figure 8A**). In other words, TREP favored consistent states *i.e.*, significantly more below GAM curve in pre-IP (lower *TRPM4* and Ribo) and above GAM curve in post-IP (higher *TRPM4* and Ribo).

3.10 Pre-IP/post-IP overlap and Ribo expression variability predict *TRPM4*-Ribo modeling outcomes

Next, to gain insights on why patients demonstrated a wide range of DE, raincloud plots were used to visualize the distribution pattern and overlap of Ribo expression levels in pre-IP versus post-IP, in Pt.1 (low DE, 31.5%) and Pt.4 (high DE, 83.5%) PCa cells (**Figure 8B**). In Pt.1, high overlap in Ribo expression levels in pre-IP and post-IP was observed (OVL=57%). In contrast, Pt.4 with high DE showed low overlap of Ribo expression (OVL=15.2%), and the pre-IP region showed a wider range of Ribo expression levels (Pt.4 pre-IP IQR: 3.2–5.1 versus Pt.1 pre-IP IQR: 5.8–6.7; **Figure 8B**). These observations indicate that higher variability in Ribo expression levels, when modeled according to *TRPM4*, resulted in higher DE. The remaining patients also showed similar characteristics where higher OVL and lower variability in Ribo expression (in pre-IP and/or post-IP) resulted in lower DE, such as in Pt.2 (OVL=66%; IQR pre-IP: 4.9–5.7, IQR post-IP: 5.5–6.6; DE=28.6%) (**Figure 8C**). The exact number of TREP and non-TREP cells in pre-IP and post-IP regions, below or above GAM curve, for each patient is presented in **Supplementary Table 12**.

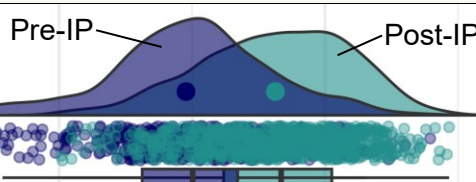
Figure 8



(B)

Pt.1 (OVL = 57%; IQR: pre-IP = 5.8-6.7, post-IP = 6.5-7.6)

DE: 31.5%



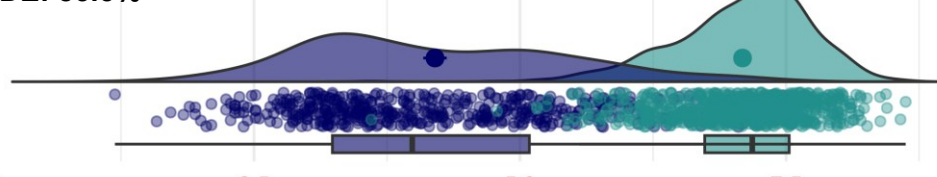
High overlap in Ribo expression levels in pre-IP vs post-IP

↓ Lower variability that can be captured by TRPM4 modeling

↓ Lower DE (31.5%) and lower number of TREP cells

Pt.4 (OVL = 15.2%; IQR: pre-IP = 3.2-5.1, post-IP = 6.7-7.5)

DE: 83.5%



Low overlap in Ribo expression levels in pre-IP vs post-IP

↓ Higher variability that can be captured by TRPM4 modeling

↓ Higher DE (83.5%) and higher number of TREP cells

0.0

2.5

5.0

7.5

Ribo expression (\log_2)

Key: Pre-IP Post-IP

(C)

Pt.2 IP: 2.21

Pt.3 IP: 3.18

Pt.5 IP: 2.64

Pt.6 IP: 3.47

Pt.7 IP: 3.48

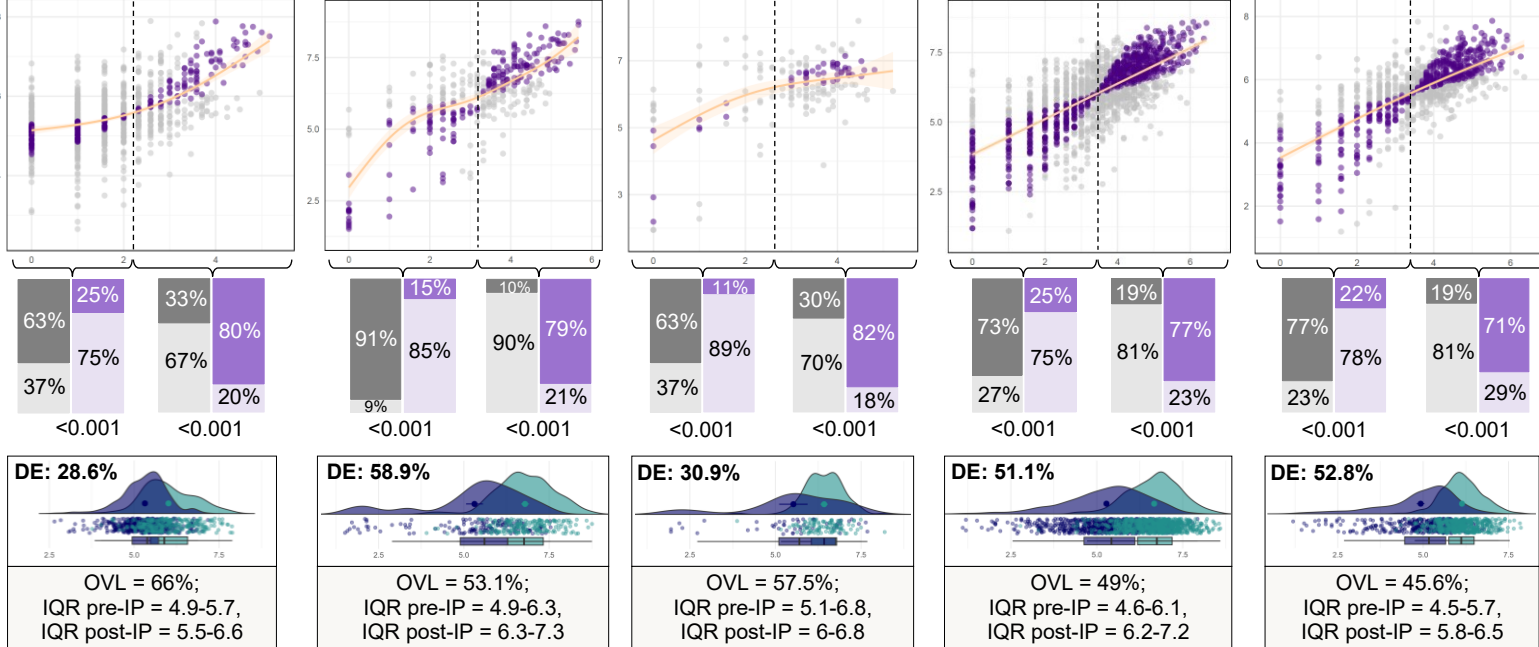


Figure 8 Characteristics of TREP and non-TREP cells in relation to GAM curves and insights on why DE% differs across patients. (A) Distribution of TREP and non-TREP cells, and the fitted GAM curve. Mosaic plots to compare the difference in the proportion of TREP vs non-TREP cells below or above the GAM curve in pre-IP (left mosaic plot placed below pre-IP region) or post-IP (right mosaic plot placed below the post-IP region). For instance, in Pt.1 (or Pt.4), significantly more TREP cells were found below or above the GAM curve in pre-IP or post-IP, respectively (FDR<0.001); (B) Raincloud plots of each cell's Ribo expression values (\log_2) according to pre-IP or post-IP in Pt.1 (top graph) and Pt.4 (bottom graph). OVL assessed the proportion of cells (%) with overlapping range of Ribo values in pre-IP and post-IP; IQR of Ribo expression values in pre-IP or post-IP; DE% of TRPM4-Ribo GAM modeling; (C) Distribution patterns of TREP and non-TREP cells along the fitted GAM curves (top graphs), mosaic plots of the proportion of TREP or non-TREP cells in pre-IP or post-IP (middle graphs), and raincloud plots of Ribo expression for each cell (bottom graphs) in the rest of the PCa patients (Pt.2, Pt.3, Pt.5, Pt.6, and Pt.7).

3.11 CEP-IP framework reveals distinct biological pathways: Ribosomal, translation, and cell adhesion GOs enriched in post-IP TREP cells

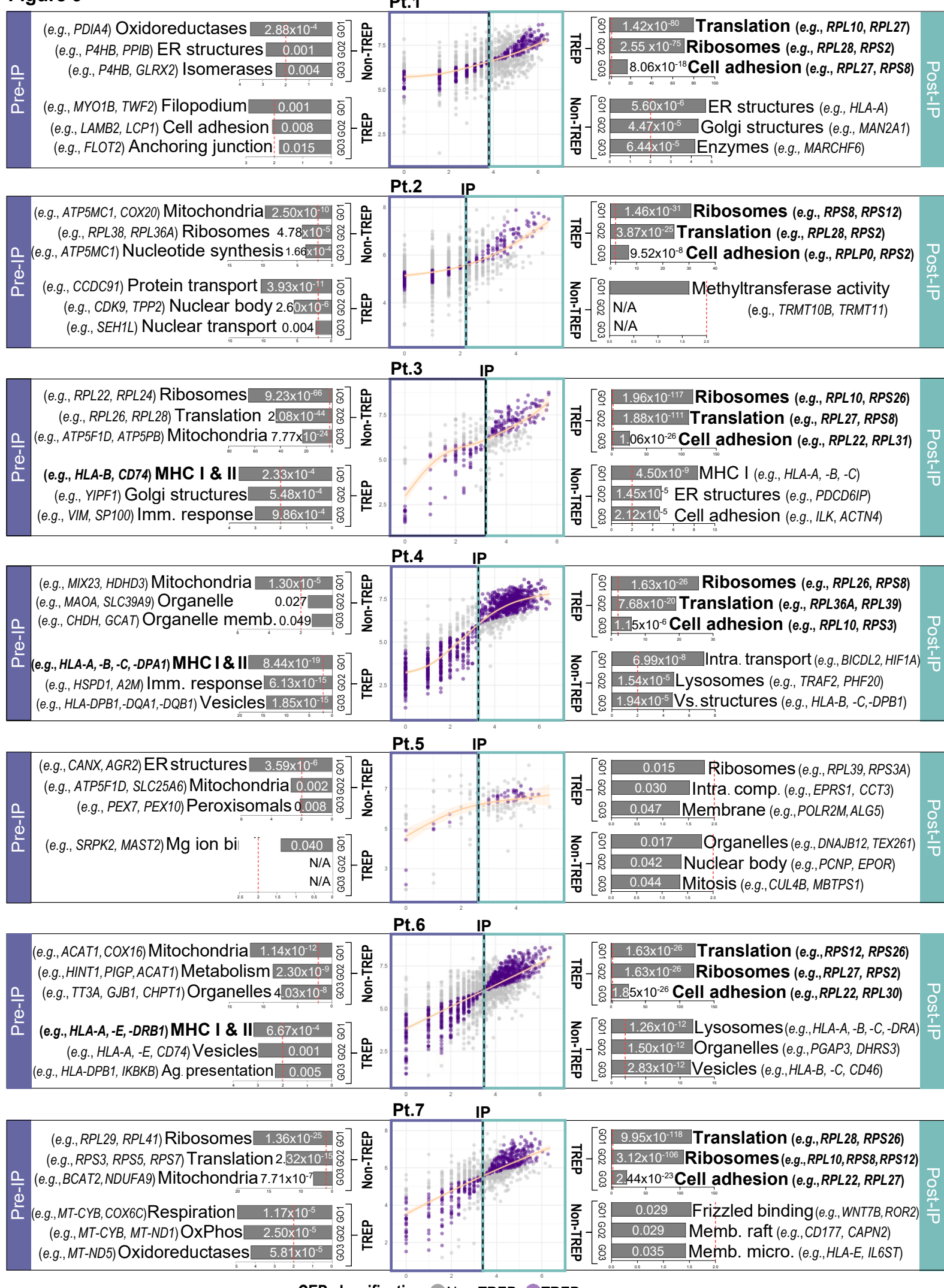
GO enrichment analysis of genes significantly upregulated in TREP or non-TREP cells, in pre-IP or post-IP, was conducted to test the potential GO differences among these four populations of PCa cells in each patient. Post-IP TREP cells in six of the seven PCa patients consistently showed significant enrichment of ribosomes, translation, and cell adhesion GOs (FDR<0.01; **Figure 9**). The upregulated genes in these three GOs primarily involved ribosomal genes, including the seven ribosomal genes within Ribo gene set such as *RPL10*, *RPL27*, *RPS2*, or *RPS8* (**Supplementary Table 13**). Post-IP TREP cells of Pt.5 showed enriched ribosome GOs only (FDR=0.015) without translation or cell adhesion GOs enrichment, potentially due to low number of TREP cells (post-IP TREP cells, n=39, while the number of post-IP TREP cells in all other patients were >50).

In pre-IP TREP cells, major histocompatibility complex (MHC) class I and II GOs were significantly enriched (FDR<0.01) in three PCa patients (Pt. 3, Pt.4, and Pt.6), whereby MHC class I and II genes such as *HLA-A*, *HLA-B*, or *CD74* were significantly upregulated. Non-TREP cells in pre-IP or post-IP yielded enrichment of mitochondria and other cellular structures (endoplasmic reticulum, lysosomes, or organelles), respectively, across majority of the PCa patients (**Figure 9** and **Supplementary Table 13**).

3.12 Pre-IP TREP cells formed distinct population of cells with post-IP TREP cells in Monocle3 trajectory

As shown in the previous section, GAM's DE potentially identified population of cells that progressed along a continuous trajectory in the *TRPM4*-Ribo transcriptional space. To test this further, Monocle3 trajectory analysis was performed to observe if pre-IP TREP cells formed distinct, yet continuous, population of cells with post-IP TREP cells along Monocle3 trajectory *i.e.*, well-separated clusters of TREP cells with intermediate TREP cells connecting both distinct populations. Qualitatively, visual inspection of the Monocle3 trajectory in UMAP1 and UMAP2 space for each patient showed distinct clusters of pre-IP TREP cells (colored in magenta) that were well-separated from post-IP TREP cells (colored in indigo), with intermediate pre-IP or post-IP TREP cells (**Figure 10**). These observations also corroborated with ridgeline plots of cells density in UMAP1 space (the Monocle3 UMAP dimension that captured the most variability) showing dissimilar yet coherent distribution of TREP cells between the pre-IP and post-IP regions. Quantitatively, magnitude of their separation in UMAP1 space was assessed whereby all patients showed significant separation of pre-IP TREP cells from post-IP TREP cells (FDR<0.05). Pt.3, Pt.4, and Pt.6 showed large magnitude of separation that was highly significant ($|\delta| \geq 0.43$; FDR<0.001).

Figure 9

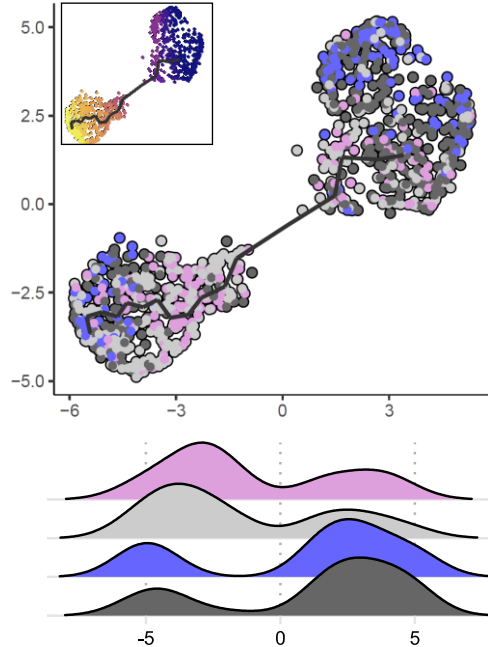


CEP classification: Non-TREP TREP

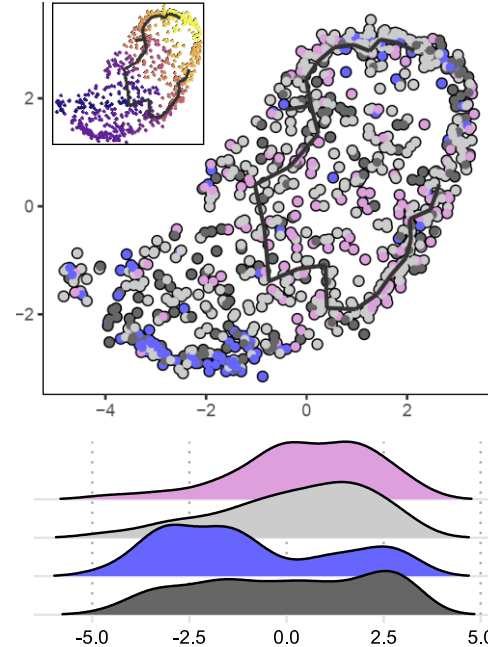
Figure 9 GOs enriched in TREP (purple) or non-TREP (gray) cells in pre-IP or post-IP of each PCa patient. The IP for each patient represents the point where more TREP cells transitioned from being found more frequently below the GAM curve to above GAM curve *i.e.*, the point separating pre-IP (purple box) from post-IP (green box). For each pre-IP and post-IP region, the cells were binarized into TREP or non-TREP cells, with each population of cells containing their own enriched GOs. Three significant GO groups (GO1-GO3) are represented in each bar graph (x-axis: $\log_{10}\text{FDR}$) with dotted red line representing $\text{FDR}=0.01$ $[-\log_{10}(0.01)=2]$ to represent a more stringent cut-off. GO groups representing ribosomes, translation, cell adhesion, and MHC class I and II GOs are in bold.

Figure 10

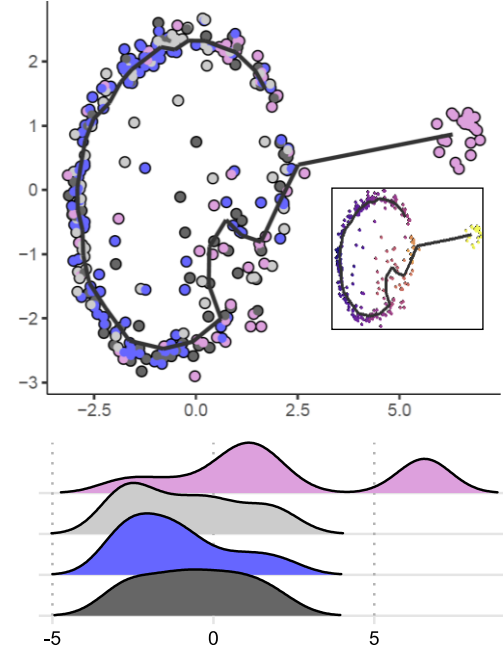
Pt.1



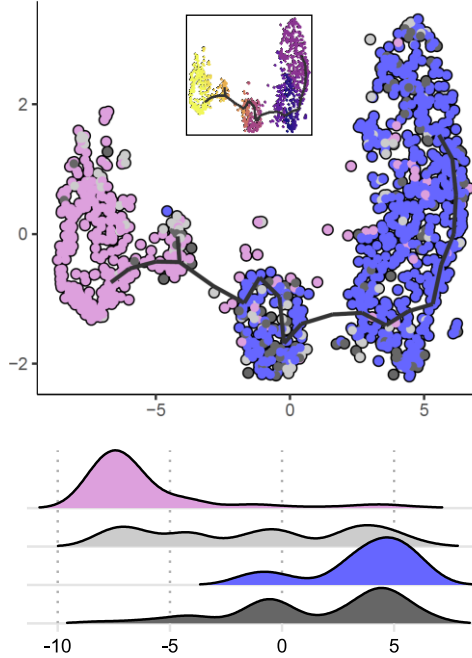
Pt.2



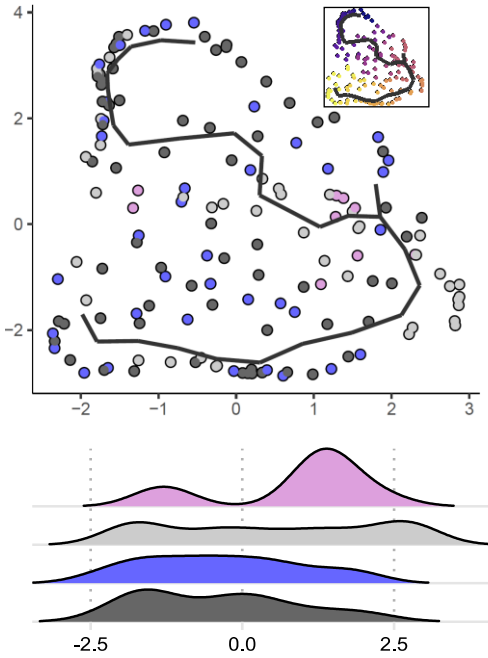
Pt.3



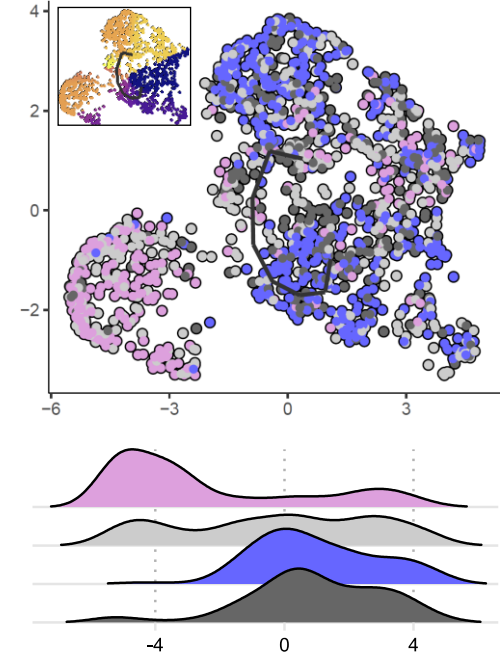
Pt.4



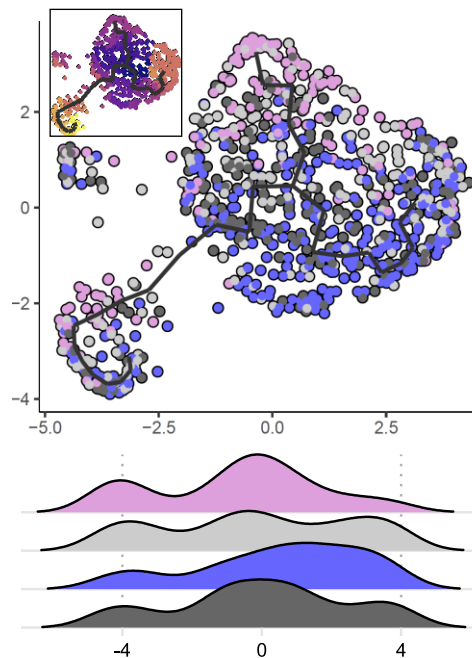
Pt.5



Pt.6



Pt.7



Pre-IP vs Post-IP TREP cells based on Monocle3 UMAP1

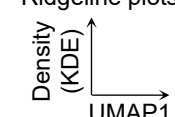
Patient	DE (%)	Monocle3 UMAP1 [median (IQR)]		Cliff's delta, $ \delta $	Magnitude of $ \delta $	FDR (UMAP1)
		Pre-IP TREP	Post-IP TREP			
Pt.1	31.5	-2.321 (5.183)	2.087 (7.598)	0.229	Small	0.001
Pt.2	28.6	0.526 (2.210)	-1.460 (3.973)	0.391	Medium	<0.001
Pt.3	58.9	1.381 (5.807)	-1.478 (2.247)	0.591	Large	<0.001
Pt.4	83.5	-7.110 (1.699)	4.296 (2.328)	0.928	Large	<0.001
Pt.5	30.9	1.291 (0.439)	-0.375 (1.976)	0.493	Large	0.021
Pt.6	51.1	-3.550 (4.838)	0.660 (2.692)	0.610	Large	<0.001
Pt.7	52.8	-0.407 (3.338)	0.878 (3.365)	0.299	Small	<0.001

Key:

All plots (cell type):

- Pre-IP TREP
- Pre-IP non-TREP
- Post-IP TREP
- Post-IP non-TREP

Ridgeline plots:



Monocle3 plots:

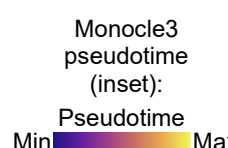
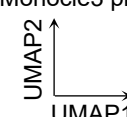


Figure 10. Distribution patterns of TREP cells in pre-IP (magenta) and post-IP (indigo) according to Monocle3 cell trajectory of the PCa cells of each patient (Pt.1–Pt.7). Monocle3 pseudotime plot (root cell: highest *TRPM4* expression) is included as an inset of the main trajectory plot. Ridgeline plot is shown below the trajectory plot according to Monocle3's UMAP1 (x-axis) and density (kernel density estimation, KDE; y-axis). Comparison of Monocle3's UMAP1 values of TREP cells in pre-IP versus post-IP is shown and magnitude of $|\delta|$ is according to established cut-offs [43]. Note that the UMAP1 axis in the ridgeline plot has been processed by KDE, which may differ from the raw UMAP1 coordinates in the trajectory plot, but their distribution patterns (i.e., density across UMAP1 axis) remain similar.

4. Discussion

The CEP-IP framework developed in this study represents a novel approach to explainable ML in single-cell analysis. The framework enables mapping for biologically significant cell subpopulations, that conventional correlation-based methods may overlook, by assigning GAM performance into cell-level contributions (CEP), combined with spatial transcriptional stratification (IP). In this section, the biological findings of the study were discussed before addressing the ML aspects.

Ribosomes consist of the large (60S) and small (40S) subunits derived from the ribosomal protein large subunit (RPL) and small subunit (RPS), respectively. Aberrant expression and derailed functions of RPL and RPS proteins have been implicated in multiple types of cancer including PCa [49-51]. For instance, RPL10 protein is decreased in early stage PCa but increased in late stage PCa cases, suggesting that reduced RPL10 expression may play roles in the development of early PCa and increased in more aggressive phenotype [52]. RPS2 is overexpressed in PCa tissues compared with BP cases [49]. In immunodeficient mice with PCa cells, tumor growth and metastasis were inhibited by targeting RPS2 and eventually eradicated, where their survival was improved by inhibiting RPS2 in a dose-dependent manner [53].

There is a paucity of information linking *TRPM4* with ribosomes in PCa. However, *TRPM4* has been associated with ribosomes in calcified aortic valves, where *TRPM4* is frequently elevated and promotes inflammation in the disease [54, 55]. *TRPM4* mRNA is post-transcriptionally regulated by the m6A reader protein YTHDF1, in which binding of YTHDF1 with the m6A site of *TRPM4* mRNA enhances stability of the transcript and increases *TRPM4* translation. This is thought to be due to increased ribosomes occupancy for *TRPM4* transcript that promotes its translation, attributable to the established roles of YTHDF1 that induces ribosomal occupancy and enhances translation [54, 56].

AR signaling pathway is a main therapeutic target in advanced PCa such as the use of AR inhibitors abiraterone and enzalutamide [57]. Accumulating evidence has demonstrated the link between AR and ribosomal proteins. In advanced PCa cases, ribosomal proteins amplification was observed, and treatment of aggressive PCa cells with histone acetyltransferase inhibitors derailed AR signaling characterized by the downregulation of ribosomal proteins [58]. Likewise, activation of AR is also dependent on the integrity of the translational machinery. For instance, inhibition of translation processes via ribosome collisions led to reduction in AR translation, enhancing AR-targeted therapy in PCa [59]. Essentially, mass spectrometry of PCa cells showed that proteins involved in translation regulation were enriched. In particular, AR transactivation was suppressed in hormone-sensitive PCa cells through translational inhibition [60]. In terms of association with *TRPM4*, treatment of PCa cells with *TRPM4* inhibitor suppressed the expression of AR protein in a dose-dependent manner, suggesting the involvement of *TRPM4* protein in AR signaling in PCa [45].

As observed in this study, the *TRPM4*-Ribo's DE was significantly higher than other signaling pathways implicated with *TRPM4* previously including GSK-3 β , mTOR, NF- κ B, PI3K/AT, and Wnt but insignificant when compared with *TRPM4*-AR's DE. The patterns of *TRPM4*-Ribo and *TRPM4*-AR GAM plots were also similar in PCa cells such as concave up (Pt.1 and Pt.2), logit (Pt.3), sigmoidal (Pt.4), and linear (Pt.6 and Pt.7). Taken together, there may exist *TRPM4*/AR/Ribo axis in PCa where the expression of AR and ribosomal genes promote one another, leading to the stabilization of *TRPM4* transcripts in PCa, that in turn may promote AR signaling and ribosomal translation. However, this remains hypothetical and requires experimental verifications.

In addition, cell adhesion GOs were consistently upregulated in TREP/post-IP cells. This is comparable with the reported function of *TRPM4* in mediating cellular adhesion such as promoting focal adhesion (FA) disassembly for cellular migration [61], and interaction of *TRPM4* with end-binding proteins also promotes *TRPM4*-mediated FA disassembly and cellular invasion [62]. In PCa cells, *TRPM4* induces PCa migration and invasion by suppressing the cell adhesion protein E-cadherin and promoting epithelial–mesenchymal transition [20]. Knockdown of the ribosomal gene *RPL19* altered the expression of cell adhesion genes in prostate cancer [63], and cell adhesion was enhanced by stabilizing integrin β 1 mRNA for translation [64], demonstrating the links between cell adhesion and ribosomes. On the other hand, MHC class I and II GOs were upregulated in TREP/pre-IP cells of Pt.3, Pt.4 and Pt.6, and these three PCa patients exhibited the largest difference between TREP/pre-IP versus TREP/post-IP in Monocle3 UMAP1 space. This indicates that PCa cells with MHC expression showed more distinct trajectory or transcriptome that may be amenable to MHC/antigen immunotherapy [65, 66], while *TRPM4* inhibitors [45, 67, 68] or ribosomal subunit inhibitors [69] may be recommended to target TREP/post-IP cells.

In terms of ML aspects, monotonic relationship of *TRPM4* expression with other genes in the transcriptome was utilized as the features selection method for modeling with GAM. Instead of more sophisticated or non-monotonic approaches [70-72], robust monotonic relationships shortlisted via dual-filtering approach were adopted for explainability, and positive monotonic relationships that indicate unidirectionality is suited for additive-based modeling such as GAM. *TRPM4* is also highly expressed in PCa cells [17, 21], suggesting the presence of other genes that share similar monotonic expression profile (co-expression) for functional synergy.

In the GAM workflow, the smooth terms dimension k was treated as a hyperparameter to optimize in PRSS, where the exploration phase tested a range of k values followed by verification phase to validate that the best k value was found. Each PRSS iteration (*i.e.*, each specific k value) was given the opportunity to optimize the smoothing parameter λ in its nested REML loop. This differs from the current approach where default or user-specified k value is used according to the `gam.check()` function that indicates whether a tested k value needs to be increased [28, 73]. PRSS was instead adopted in this study as the objective function to obtain the best k value due to its objective nature for model comparison, without the requirement for manual re-specification and refitting with another k value. By treating k as a search space, it allows for the exploration of a broad range of k values, and this approach complements existing diagnostic tools.

The penalty multiplier γ was optimized by testing a range of γ values in 0.5 increments and visualizing the GAM curves for signs of suboptimal fitting. Automated optimization such as treating γ as a hyperparameter space, or with metrics such as generalized cross-validation, was not conducted in favor of visual inspection. As the end-product is the fitted GAM curve, visual inspection provides direct assessment of whether the fitted curve fluctuates or with steep slopes, particularly in areas with sparse cell numbers that may represent artifacts in scRNA-seq data [74, 75]. The selected γ value of 1.5 in this study aligns with the γ value of 1.4 recommended in `mgcv` package documentation to reduce overfitting [42].

GOs enriched in PCa cells utilizing Sperman-Kendall's dual-filter, without segregating into subtypes based on TREP/IP status, showed that *TRPM4* may play roles in the regulation of protein localization and transporter complexes with significance level of approximately FDR=0.01 (**Figure 1E**). When the PCa cells were subtyped into four populations, translation, ribosomal and cellular adhesion processes were consistently upregulated in TREP/post-IP cells with stronger level of significance (FDR<1x10⁻⁵) (**Figure 7**). This aligns with GAM-identified TREP/IP cells which formed spatially dissimilar clusters in Monocle3 trajectory space. Moreover, GAM's DE prioritized cells in consistent states where both *TRPM4* and Ribo were either lower or higher, giving less weight to cells with inconsistent *TRPM4*-Ribo relationship that may represent transitional cells, outliers, or with complex variation influenced by other factors beyond the relationship being modeled. It was also observed that GAM did not simply take into account cells located closely along the GAM curve to map for TREP cells, but instead considered cells that contributed to the overall shape of the fitted curve globally. This may improve the likelihood of identifying biologically relevant cells with preserved functional relationships, and to map for cells that may follow a continuous developmental trajectory into distinct states. Collectively, these observations imply that GAM-derived cell states are potentially biologically relevant, not captured by conventional correlation thresholds but revealed by GAM and TREP/IP grouping in *TRPM4*-Ribo space.

The IP represents the key transition point (*i.e.*, specific *TRPM4* value) where the distribution pattern of TREP cells shifted, stratifying the cells into the pre-IP and post-IP regions. This enables the following insights: (i) GAM's DE prioritizing cells with consistent expression states; (ii) Explanation of why patients demonstrated lower or higher DE in their modeling; (iii) Stratification of cells into four groups for GO enrichment analysis to inform potential targeted therapies for each group of cells. The IP status differs from conventional gene expression analysis approaches, where fixed thresholds are often used such as fold-change cutoffs or fixed ranks [76-78]. In GAM analysis, the IP cut-off is rooted in the overall shape of the fitted curve that leverages the flexibility of splines to account for non-linearity in the modeled relationship. Instead of adopting uniform thresholds across the patients, the IP approach produces patient-specific transition points, reflecting potential underlying biological relationship, cellular populations heterogeneity, and progression trajectory.

GAM has recently been adopted to analyze scRNA-seq data, primarily for cellular trajectories analysis [35, 79, 80]. The tradeSeq algorithm models gene expression with pseudotime utilizing GAM to identify DEGs between lineages along pseudotime trajectories, allowing the inference of gene expression changes during development [35]. This is conceptually different from this study's approach, whereby the gene expression relationship between two variables (*e.g.*, *TRPM4* and Ribo) were first modeled to identify the underlying shape, before determining which specific cell contributed to this relationship via their individual contribution magnitude to the model's DE. This subsequently enables subtyping of cells into different biological states by incorporating the IP spatial dimension. In addition, tradeSeq requires pre-computed trajectories as input for GAM analysis to identify lineage-specific genes. This is distinct from this study that uses monotonic, dual-filtered genes as input for GAM to identify cell populations that drive (or do not drive) the modeled relationship, and implementing them as input for cross-platform trajectory validation.

The limitations of the current study, and the future opportunities that they represent, are acknowledged as follows:

- i) The presence of a specific shape of the relationship being modeled was assumed, and such a relationship may not exist in the first place. However, without attempts to unravel the potential nature of their relationship, the investigation stops at the simple monotonic level, which obscures potential non-linearity and underlying biology.
- ii) Cell populations with insufficient number of cells (*e.g.*, <50 cells) resulted in unreliable enrichment of GOs, as exemplified by Pt.5's TREP/post-IP cell population that did not

exhibit enrichment of GOs consistently shared by the rest of the patients. For such scenarios, it is suggested to adopt patient-specific dual-filtered genes, instead of the pan-patient filtering approach employed in this study.

iii) GAM's DE is an aggregate metric of residuals from individual cells. The CEP classification was designed as attempts to decompose the aggregate model performance into individual cell contributions, providing cell-level explainability for GAM models. However, this is not a complete decomposition due to individual EP values that do not sum exactly to GAM's DE. Hence, CEP is primarily a method to identify cells most well-predicted by the model, instead of identifying cells most contributive to the overall DE.

iv) Three patients in this study (Pt.3, Pt.4, and Pt.6), showed consensus GOs in their pre-IP and post-IP TREP cells, with clear separation of pre-IP and post-IP TREP cells in Monocle3 trajectory space. Hence, GAM modeling can delineate underlying biology of well-predicted cells (*i.e.*, TREP cells) in cases with strong pairwise relationships (*e.g.*, DE >50%). However, Pt.7 showed dissimilar GOs in their pre-IP TREP cells (no enrichment of MHC GOs) despite DE of 52.8% and with consensus GOs for post-IP TREP cells. This highlights the ongoing challenge posed by cancer cells heterogeneity, as well as the limitations of pairwise gene relationship modeling that does not take into account additional genes or regulatory factors that may further explain biological distinctions. Nevertheless, this study was designed to focus on pairwise gene relationship modeling, without diluting the focus with additional variables because another aim was to explore GAM's mechanisms and touted explainability, aligning with the XAI approach where ML models are encouraged to be explainable for safe deployment [81-83].

v) Experimental wet-lab validations beyond in silico modeling and pathway analysis are required to confirm that GAM-identified cell populations represent actual biological states.

vi) Complete automation of the workflow in this study remains challenging, as manual methods were required, including γ parameter optimization, visual inspection of IP, and GO enrichment interpretation. Nonetheless, these manual interventions necessitate study-specific optimization, which encourages deeper understanding of the algorithm's mechanisms and explainability in the process.

In conclusion, the CEP-IP framework (*i.e.*, mapping for TREP or non-TREP cells in pre-IP or post-IP regions) produces quadrants of cell subpopulations. These four groups show distinct gene expression profiles and biological pathways that may inform specific therapeutic choices. While demonstrated in this study with *TRPM4*-ribosome relationships in PCa, the CEP-IP framework is applicable for other settings, whereby any pairwise genes of interest in specific diseases can be inputted to generate similar quadrants for downstream applications. The CEP-IP framework's flexible splines through GAMs unravel the biological relationships between pairwise genes, providing a novel XAI framework for single-cell analysis with therapeutic implications.

Data and Code Availability

Supplementary Tables 1 to 13 (Excel format) are available on Zenodo: <https://zenodo.org/records/17114394>

The processed Seurat object GSE185344_Seurat_processed.RData (9.52 GB) is available on HuggingFace:

https://huggingface.co/datasets/kahkengwong/CEP-IP_Framework

The code used in this project is available on GitHub:
https://github.com/kahkengwong/CEP-IP_Framework

The following blocks of code are available in the GitHub repository:

```
Part_1_scRNAseq_preprocessing_and_UMAP_clusters.r
Part_2_UMAP_Heatmap_Spearman-Kendall's-matrix.r
Part_3.01_Mean_Expression_Justifications.r
Part_3.02_Family_Distribution_Analysis.r
Part_3.03_GAM_REML_PRSS_Setup.r
Part_3.04_GAM_REML_PRSS_Analysis.r
Part_3.05_REML_Extraction_and_Convergence.r
Part_3.06_REML_PRSS_Plots_and_EDF_Analysis.r
Part_3.07_Validation_of_k_and_Lambda_Selection.r
Part_3.08_Visualize_TPRS_and_GAM_Components.r
Part_3.09_Extract_GAM's_ND_MD_DE.r
Part_3.10_Extract_TRPM4-Ribo_EP.r
Part_3.11_MCCV_of_CEP_Classification.r
Part_3.12_CEP-IP_GAM_Plots.r
Part_3.13_CEP-IP_Mosaic_and_Raincloud_Plots.r
Part_3.14_CEP-IP_DEGs_Analysis.r
Part_3.15_CEP-IP_in_Monocle3_Trajectory.r
```

The R packages and versions used in this study were saved in the `renv.lock` file included in the GitHub repository. This lockfile contains version information for all 37 packages used with their dependencies. Clone the repository and run `renv::restore()` to install the identical package versions used in this study. Note that `renv` creates an isolated library and will not modify a system's existing R packages and setup. For manual or selected package installation, a simplified `r_packages_info.json` file is provided with the package names, versions, and sources (CRAN, Bioconductor, or GitHub).

CRediT authorship contribution statement

Kah Keng Wong: Conceptualization, Funding acquisition, Resources, Data curation, Investigation, Formal analysis, Software, Validation, Visualization, Supervision, Writing – original draft, Writing – review & editing.

Declaration of competing interest

The author declares that the research was conducted in the absence of any commercial or financial relationships that could be construed as a potential conflict of interest.

Acknowledgements

This work was supported by the Research University Grant (1001/PPSP/8012349), Universiti Sains Malaysia awarded to Kah Keng Wong. The author extends heartfelt thanks to the School of Medical Sciences and Research Creativity & Management Office (RCMO), Universiti Sains Malaysia, for their invaluable support.

References

- [1] Sung H, Ferlay J, Siegel RL *et al.* Global cancer statistics 2020: GLOBOCAN estimates of incidence and mortality worldwide for 36 cancers in 185 countries. *CA Cancer J Clin* **71**:209-249 (2021).
- [2] Siegel RL, Miller KD, Wagle NS *et al.* Cancer statistics, 2023. *CA Cancer J Clin* **73**:17-48 (2023).
- [3] Serda-Ferrer BC, Sanvisens A, Fuentes-Raspall R *et al.* Significantly reduced incidence and improved survival from prostate cancer over 25 years. *BMC Public Health* **23**:2552 (2023).

[4] Wu JN, Fish KM, Evans CP *et al.* No improvement noted in overall or cause-specific survival for men presenting with metastatic prostate cancer over a 20-year period. *Cancer* **120**:818-823 (2014).

[5] Crawford ED, Petrylak D, Sartor O. Navigating the evolving therapeutic landscape in advanced prostate cancer. *Urol Oncol* **35**:S1-S13 (2017).

[6] Nilius B, Mahieu F, Prenen J *et al.* The Ca²⁺-activated cation channel TRPM4 is regulated by phosphatidylinositol 4,5-biphosphate. *EMBO J* **25**:467-478 (2006).

[7] Demion M, Bois P, Launay P *et al.* TRPM4, a Ca²⁺-activated nonselective cation channel in mouse sino-atrial node cells. *Cardiovasc Res* **73**:531-538 (2007).

[8] Bianchi B, Ozhathil LC, Medeiros-Domingo A *et al.* Four TRPM4 cation channel mutations found in cardiac conduction diseases lead to altered protein stability. *Front Physiol* **9**:177 (2018).

[9] Chen B, Ng G, Gao Y *et al.* Non-invasive multimodality imaging directly shows TRPM4 inhibition ameliorates stroke reperfusion injury. *Transl Stroke Res* **10**:91-103 (2019).

[10] Arullampalam P, Essers MC, Boukenna M *et al.* Knockdown of the TRPM4 channel alters cardiac electrophysiology and hemodynamics in a sex- and age-dependent manner in mice. *Physiol Rep* **11**:e15783 (2023).

[11] Hedon C, Lambert K, Chakouri N *et al.* New role of TRPM4 channel in the cardiac excitation-contraction coupling in response to physiological and pathological hypertrophy in mouse. *Prog Biophys Mol Biol* **159**:105-117 (2021).

[12] Wong KK, Hussain FA. TRPM4 is overexpressed in breast cancer associated with estrogen response and epithelial-mesenchymal transition gene sets. *PLoS One* **15**:e0233884 (2020).

[13] Guo J, Liu F, Yang X *et al.* TRPM4 channels contribute to Adriamycin chemoresistance in breast cancer cells. *Eur J Pharmacol* **998**:177637 (2025).

[14] Suguro M, Tagawa H, Kagami Y *et al.* Expression profiling analysis of the CD5+ diffuse large B-cell lymphoma subgroup: development of a CD5 signature. *Cancer Sci* **97**:868-874 (2006).

[15] Loo SK, Ch'ng ES, Md Salleh MS *et al.* TRPM4 expression is associated with activated B cell subtype and poor survival in diffuse large B cell lymphoma. *Histopathology* **71**:98-111 (2017).

[16] Schinke EN, Bii V, Nalla A *et al.* A novel approach to identify driver genes involved in androgen-independent prostate cancer. *Mol Cancer* **13**:120 (2014).

[17] Berg KD, Soldini D, Jung M *et al.* TRPM4 protein expression in prostate cancer: a novel tissue biomarker associated with risk of biochemical recurrence following radical prostatectomy. *Virchows Arch* **468**:345-355 (2016).

[18] Holzmann C, Kappel S, Kilch T *et al.* Transient receptor potential melastatin 4 channel contributes to migration of androgen-insensitive prostate cancer cells. *Oncotarget* **6**:41783-41793 (2015).

[19] Hong X, Yu JJ. MicroRNA-150 suppresses epithelial-mesenchymal transition, invasion, and metastasis in prostate cancer through the TRPM4-mediated beta-catenin signaling pathway. *Am J Physiol Cell Physiol* **316**:C463-C480 (2019).

[20] Sagredo AI, Sagredo EA, Pola V *et al.* TRPM4 channel is involved in regulating epithelial to mesenchymal transition, migration, and invasion of prostate cancer cell lines. *J Cell Physiol* **234**:2037-2050 (2019).

[21] Wong KK, Banham AH, Yaacob NS *et al.* The oncogenic roles of TRPM ion channels in cancer. *J Cell Physiol* **234**:14556-14573 (2019).

[22] Bochen F, Subedi S, La Manna F *et al.* TRPM4 contributes to cell death in prostate cancer tumor spheroids, and to extravasation and metastasis in a zebrafish xenograft model system. *Mol Oncol* **19**:1299-1309 (2025).

[23] Borgstrom A, Hauert B, Kappel S *et al.* Small molecular inhibitors block TRPM4 currents in prostate cancer cells, with limited impact on cancer hallmark functions. *J Mol Biol* **433**:166665 (2021).

[24] Wood SN. On confidence intervals for generalized additive models based on penalized regression splines. *Aust N Z J Stat* **48**:445-464 (2006).

[25] Wood SN. Fast stable restricted maximum likelihood and marginal likelihood estimation of semiparametric generalized linear models. *J R Stat Soc Ser B Stat Methodol* **73**:3-36 (2011).

[26] Wood SN. Generalized additive models: an introduction with R. *Second Edition Boca Raton: CRC Press* (2017).

[27] Wood SN, Goude Y, Shaw S. Generalized additive models for large data sets. *J R Stat Soc Series C Appl Stat* **64**:139-155 (2015).

[28] Pedersen EJ, Miller DL, Simpson GL *et al.* Hierarchical generalized additive models in ecology: an introduction with mgcv. *PeerJ* **7**:e6876 (2019).

[29] Zhang J, Zhi M, Zhang Y. Combined generalized additive model and random forest to evaluate the influence of environmental factors on phytoplankton biomass in a large eutrophic lake. *Ecol Indic* **130**:108082 (2021).

[30] Pachauri N, Ahn CW. Electrical energy prediction of combined cycle power plant using gradient boosted generalized additive model. *IEEE Access* **10**:24566-24577 (2022).

[31] Sundararajan A, Ollis B. Regression and generalized additive model to enhance the performance of photovoltaic power ensemble predictors. *IEEE Access* **9**:111899-111914 (2021).

[32] Wood SN, Li Z, Shaddick G *et al.* Generalized additive models for gigadata: modeling the UK black smoke network daily data. *JASA* **112**:1199-1210 (2017).

[33] Huang X, Ma W, Law C *et al.* Importance of applying mixed generalized additive model (MGAM) as a method for assessing the environmental health impacts: Ambient temperature and acute myocardial infarction (AMI), among elderly in Shanghai, China. *PLoS One* **16**:e0255767 (2021).

[34] Xiong S, Wu A, Weng L *et al.* Study on the correlation between the number of mushroom poisoning cases and meteorological factors based on the generalized additive model in Guizhou Province, 2023. *BMC Public Health* **24**:2628 (2024).

[35] Van den Berge K, Roux de Bézieux H, Street K *et al.* Trajectory-based differential expression analysis for single-cell sequencing data. *Nat Commun* **11**:1201 (2020).

[36] Song D, Li JJ. PseudotimeDE: inference of differential gene expression along cell pseudotime with well-calibrated p-values from single-cell RNA sequencing data. *Genome Biol* **22**:124 (2021).

[37] Wong HY, Sheng Q, Hesterberg AB *et al.* Single cell analysis of cribriform prostate cancer reveals cell intrinsic and tumor microenvironmental pathways of aggressive disease. *Nat Commun* **13**:6036 (2022).

[38] Satija R, Farrell JA, Gennert D *et al.* Spatial reconstruction of single-cell gene expression data. *Nat Biotechnol* **33**:495-502 (2015).

[39] Wong KK, Ab. Hamid SS. Multiomics in silico analysis identifies TM4SF4 as a cell surface target in hepatocellular carcinoma. *PLoS One* **20**:e0307048 (2025).

[40] Chen J, Bardes EE, Aronow BJ *et al.* ToppGene Suite for gene list enrichment analysis and candidate gene prioritization. *Nucleic Acids Res* **37**:W305-311 (2009).

[41] Wood SN. Inference and computation with generalized additive models and their extensions. *TEST* **29**:307-339 (2020).

[42] Wood SN. Package ‘mgcv’: Mixed GAM Computation Vehicle with Automatic Smoothness Estimation. R package version 1.9.1. <https://cran.r-project.org/web/packages/mgcv/mgcv.pdf> (2025).

[43] Meissel K, Yao ES. Using Cliff’s delta as a non-parametric effect size measure: an accessible web app and R tutorial. *PARE* **29** (2024).

[44] Chen X, Augello MA, Liu D *et al.* Canonical androgen response element motifs are tumor suppressive regulatory elements in the prostate. *Nat Commun* **15**:10675 (2024).

[45] Niu L, Liu H, Li X *et al.* Design, synthesis, and biological evaluation of 2-(naphthalen-1-yloxy)-N-phenylacetamide derivatives as TRPM4 inhibitors for the treatment of prostate cancer. *Bioorg Med Chem* **98**:117584 (2024).

[46] Sagredo AI, Sagredo EA, Cappelli C *et al.* TRPM4 regulates Akt/GSK3-beta activity and enhances beta-catenin signaling and cell proliferation in prostate cancer cells. *Mol Oncol* **12**:151-165 (2018).

[47] Li XC, Cheng Y, Yang X *et al.* Decreased expression of TRPM4 is associated with unfavorable prognosis and aggressive progression of endometrial carcinoma. *Am J Transl Res* **12**:3926-3939 (2020).

[48] Wang F, Wu P, Gong S *et al.* Aberrant TRPM4 expression in MLL-rearranged acute myeloid leukemia and its blockade induces cell cycle arrest via AKT/GLI1/Cyclin D1 pathway. *Cell Signal* **72**:109643 (2020).

[49] El Khoury W, Nasr Z. Deregulation of ribosomal proteins in human cancers. *Biosci Rep* **41**:BSR20211577 (2021).

[50] Yi X, Zhang C, Liu B *et al.* Ribosomal protein L22-like1 promotes prostate cancer progression by activating PI3K/Akt/mTOR signalling pathway. *J Cell Mol Med* **27**:403-411 (2023).

[51] Li H, He Y, Jiang J *et al.* CRISPR screening reveals that RNA helicase DDX41 triggers ribosome biogenesis and cancer progression through R-loop-mediated RPL/RPS transcription. *Nat Commun* **16**:7409 (2025).

[52] Altinok G, Powell IJ, Che M *et al.* Reduction of QM protein expression correlates with tumor grade in prostatic adenocarcinoma. *Prostate Cancer Prostatic Dis* **9**:77-82 (2006).

[53] Wang M, Hu Y, Stearns ME. RPS2: a novel therapeutic target in prostate cancer. *J Exp Clin Cancer Res* **28**:6 (2009).

[54] Wu J, Huang H, Yang W *et al.* TRPM4 mRNA stabilization by METTL3-mediated m6A modification promotes calcific aortic valve inflammation. *Helijon* **10**:e31871 (2024).

[55] Aize M, Roussel BD, Boileve A *et al.* New insights in osteogenic differentiation of human valvular interstitial cells: Implication of transient receptor potential melastatin 4 (TRPM4). *Arch Cardiovasc Dis* **117**:S196-S197 (2024).

[56] Sheth U, Parker R. Decapping and decay of messenger RNA occur in cytoplasmic processing bodies. *Science* **300**:805-808 (2003).

[57] Attard G, Murphy L, Clarke NW *et al.* Abiraterone acetate and prednisolone with or without enzalutamide for high-risk non-metastatic prostate cancer: a meta-analysis of primary results from two randomised controlled phase 3 trials of the STAMPEDE platform protocol. *Lancet* **399**:447-460 (2022).

[58] Furlan T, Kirchmair A, Sampson N *et al.* MYC-mediated ribosomal gene expression sensitizes enzalutamide-resistant prostate cancer cells to EP300/CREBBP inhibitors. *Am J Pathol* **191**:1094-1107 (2021).

[59] Cordova RA, Elbanna M, Rupert C *et al.* Caloric restriction enhances the efficacy of anti-androgen therapy in prostate cancer by inhibiting androgen receptor translation. *Cancer Res* (2025).

[60] Israel JS, Marcellin LM, Mehralivand S *et al.* The impact of androgen-induced translation in modulating androgen receptor activity. *Biol Direct* **19**:111 (2024).

[61] Caceres M, Ortiz L, Recabarren T *et al.* TRPM4 is a novel component of the adhesome required for focal adhesion disassembly, migration and contractility. *PLoS One* **10**:e0130540 (2015).

[62] Blanco C, Morales D, Mogollones I *et al.* EB1- and EB2-dependent anterograde trafficking of TRPM4 regulates focal adhesion turnover and cell invasion. *FASEB J* **33**:9434-9452 (2019).

[63] Bee A, Brewer D, Beesley C *et al.* siRNA knockdown of ribosomal protein gene RPL19 abrogates the aggressive phenotype of human prostate cancer. *PLoS One* **6**:e22672 (2011).

[64] Li E, Wei B, Wang X *et al.* METTL3 enhances cell adhesion through stabilizing integrin beta1 mRNA via an m6A-HuR-dependent mechanism in prostatic carcinoma. *Am J Cancer Res* **10**:1012-1025 (2020).

[65] Wu X, Li T, Jiang R *et al.* Targeting MHC-I molecules for cancer: function, mechanism, and therapeutic prospects. *Mol Cancer* **22**:194 (2023).

[66] Wang J, Lu Q, Chen X *et al.* Targeting MHC-I inhibitory pathways for cancer immunotherapy. *Trends Immunol* **45**:177-187 (2024).

[67] Ekundayo B, Arullampalam P, Gerber CE *et al.* Identification of a binding site for small molecule inhibitors targeting human TRPM4. *Nat Commun* **16**:833 (2025).

[68] Binkle-Ladisch L, Pironet A, Zaliani A *et al.* Identification and development of TRPM4 antagonists to counteract neuronal excitotoxicity. *iScience* **27**:111425 (2024).

[69] Zhang Z, Liu Z, Zhao W *et al.* tRF-19-W4PU732S promotes breast cancer cell malignant activity by targeting inhibition of RPL27A (ribosomal protein-L27A). *Bioengineered* **13**:2087-2098 (2022).

[70] Reshef DN, Reshef YA, Finucane HK *et al.* Detecting novel associations in large data sets. *Science* **334**:1518-1524 (2011).

[71] Chaudhuri A, Hu W. A fast algorithm for computing distance correlation. *CSDA* **135**:15-24 (2019).

[72] Chatterjee S. A new coefficient of correlation. *JASA* **116**:2009-2022 (2021).

[73] Wiley M, Wiley JF. Advanced R statistical programming and data models: Analysis, machine learning, and visualization. *Berkeley, CA: Apress* (2019).

[74] Zhang R, Atwal GS, Lim WK. Noise regularization removes correlation artifacts in single-cell RNA-seq data preprocessing. *Patterns* **2**:100211 (2021).

[75] Bacher R, Chu LF, Argus C *et al.* Enhancing biological signals and detection rates in single-cell RNA-seq experiments with cDNA library equalization. *Nucleic Acids Res* **50**:e12 (2022).

[76] Wong KK, Gascoyne DM, Soilleux EJ *et al.* FOXP2-positive diffuse large B-cell lymphomas exhibit a poor response to R-CHOP therapy and distinct biological signatures. *Oncotarget* **7**:52940-52956 (2016).

[77] Loo SK, Ab Hamid SS, Musa M *et al.* DNMT1 is associated with cell cycle and DNA replication gene sets in diffuse large B-cell lymphoma. *Pathol Res Pract* **214**:134-143 (2018).

[78] Brown PJ, Wong KK, Felce SL *et al.* FOXP1 suppresses immune response signatures and MHC class II expression in activated B-cell-like diffuse large B-cell lymphomas. *Leukemia* **30**:605-616 (2016).

[79] Maulding ND, Seninge L, Stuart JM. Associating transcription factors to single-cell trajectories with DREAMIT. *Genome Biol* **25**:220 (2024).

[80] Li X, Rao K, Chen C *et al.* A cell type and state specific gene regulation network inference method for immune regulatory analysis. *NPJ Syst Biol Appl* **11**:94 (2025).

[81] Atakishiyev S, Salameh M, Yao H *et al.* Explainable artificial intelligence for autonomous driving: A comprehensive overview and field guide for future research directions. *IEEE Access* **12**:101603-101625 (2024).

[82] Liu X, Sangers TE, Nijsten T *et al.* Predicting skin cancer risk from facial images with an explainable artificial intelligence (XAI) based approach: a proof-of-concept study. *EClinicalMedicine* **71**:102550 (2024).

[83] Nikiforidis K, Kyrtsgoglou A, Vafeiadis T *et al.* Enhancing transparency and trust in AI-powered manufacturing: A survey of explainable AI (XAI) applications in smart manufacturing in the era of industry 4.0/5.0. *ICT Express* **11**:135-148 (2025).

Supplementary Tables and Figures

Supplementary Table 1. The number and proportion of cells before and after each QC step in the scRNA-seq processing workflow, and the top 50 marker genes representing each cluster of the PCa and NonCa cases.

Supplementary Table 2. Cell count by cluster, and comparison of *TRPM4* expression between PCa clusters in NonCa and PCa cases.

Supplementary Table 3. List of *TRPM4*-monotonic genes in IBP (internal BP cells in PCa cases) and PCa cells, and the gene sets enriched by dual-filtered genes in PCa cells.

Supplementary Table 4. List of *RPL10*-, *RPL27*-, *RPL28*-, *RPS2*-, *RPS8*-, *RPS12*-, and *RPS26*-monotonic genes in PCa cells (shortlisted via Spearman–Kendall's dual-filter), and the *TRPM4*-containing gene sets enriched according to the seven ribosomal genes in PCa cells.

Supplementary Table 5. Assessment of the reliability to averaging ribosomal or AR genes into their averaged gene set (Ribo or AR) for downstream modeling.

Supplementary Table 6. Data distribution family comparison according to AIC, BIC, and DE, and the best distribution families according to AIC and BIC.

Supplementary Table 7. PRSS iterations in GAM of BP and PCa cells, REML iterations of the best GAM models of BP and PCa cells, best model's REML convergence information, and independent GAM fitting with predetermined λ values and the resulting REML scores in *TRPM4*-Ribo modeling of Pt.6 PCa cells.

Supplementary Table 8. GAM model optimization results and statistical performance metrics across different γ values tested in 0.5 increment (γ tested: 0.5–3.0).

Supplementary Table 9. GAM of all gene sets tested (AR, GSK-3 β , mTOR, NF- κ B, PI3K/AKT, and Wnt; γ =1.5), their statistical performance metrics, the observed and GAM-predicted gene set values in each cell ($n = 5,855$ cells \times 7 gene sets = 40,985 data points), and smooth basis functions' coefficient values for all modeled *TRPM4*-gene sets in each cell ($n=40,985$ data points).

Supplementary Table 10. GAM's ND, MD, and DE data for each *TRPM4*-gene set modeling, as well as each *TRPM4*-Ribo cells' EP value, ranking according to EP, and TREP or non-TREP cell status ($n=5,855$ cells).

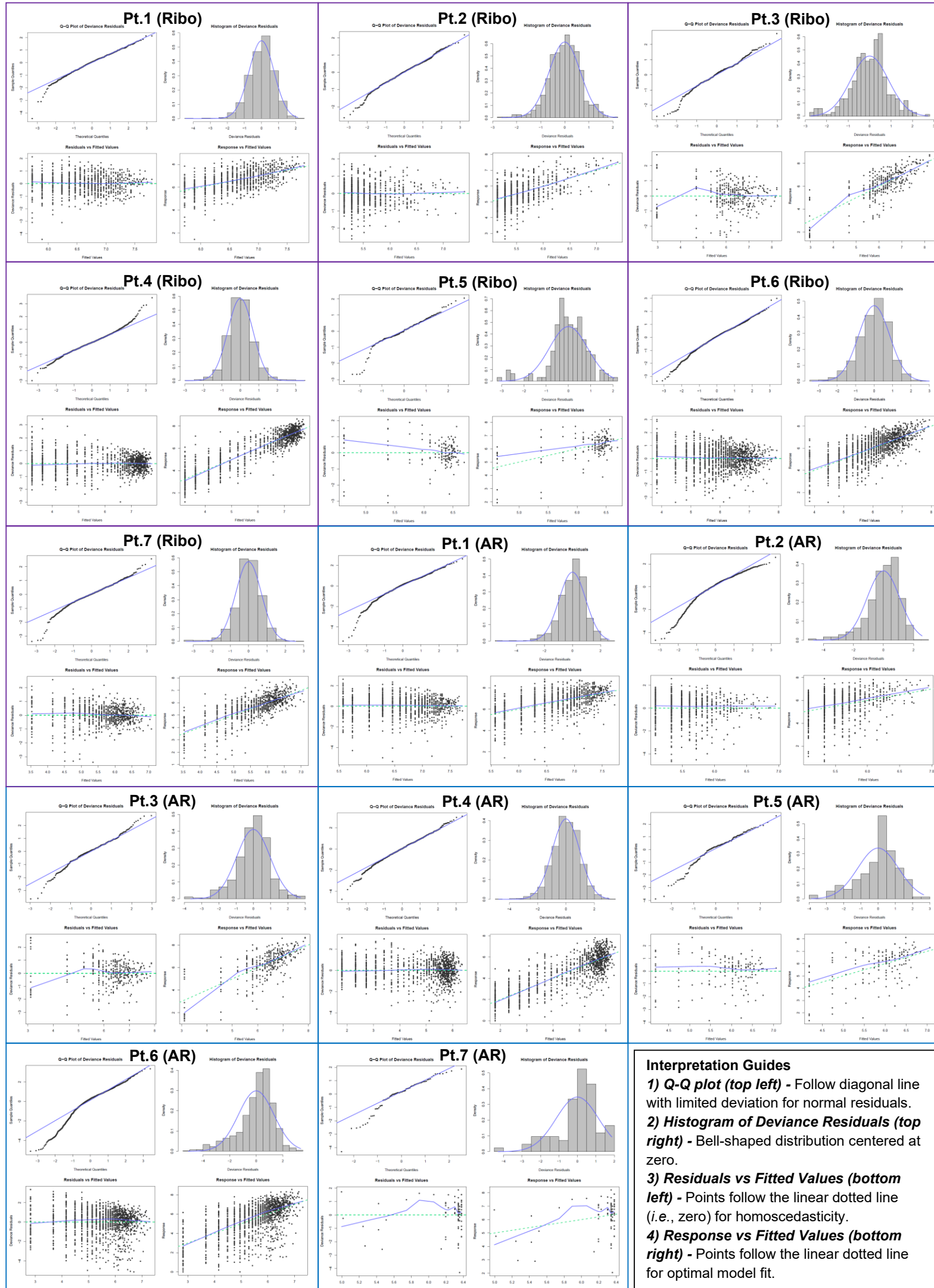
Supplementary Table 11. MCCV analysis of random, leverage, and CEP classification of PCa cells into TREP and non-TREP.

Supplementary Table 12. Number of TREP (purple in GAM plots) and non-TREP (gray in GAM plots) cells in pre-IP and post-IP, below or above GAM curves, of *TRPM4*-Ribo modeling in PCa cells.

Supplementary Table 13. GOs enriched in four populations of cells (TREP or non-TREP in pre-IP or post-IP) of each PCa patient, and the upregulated DEGs in each population of cells contributing to their enrichment.

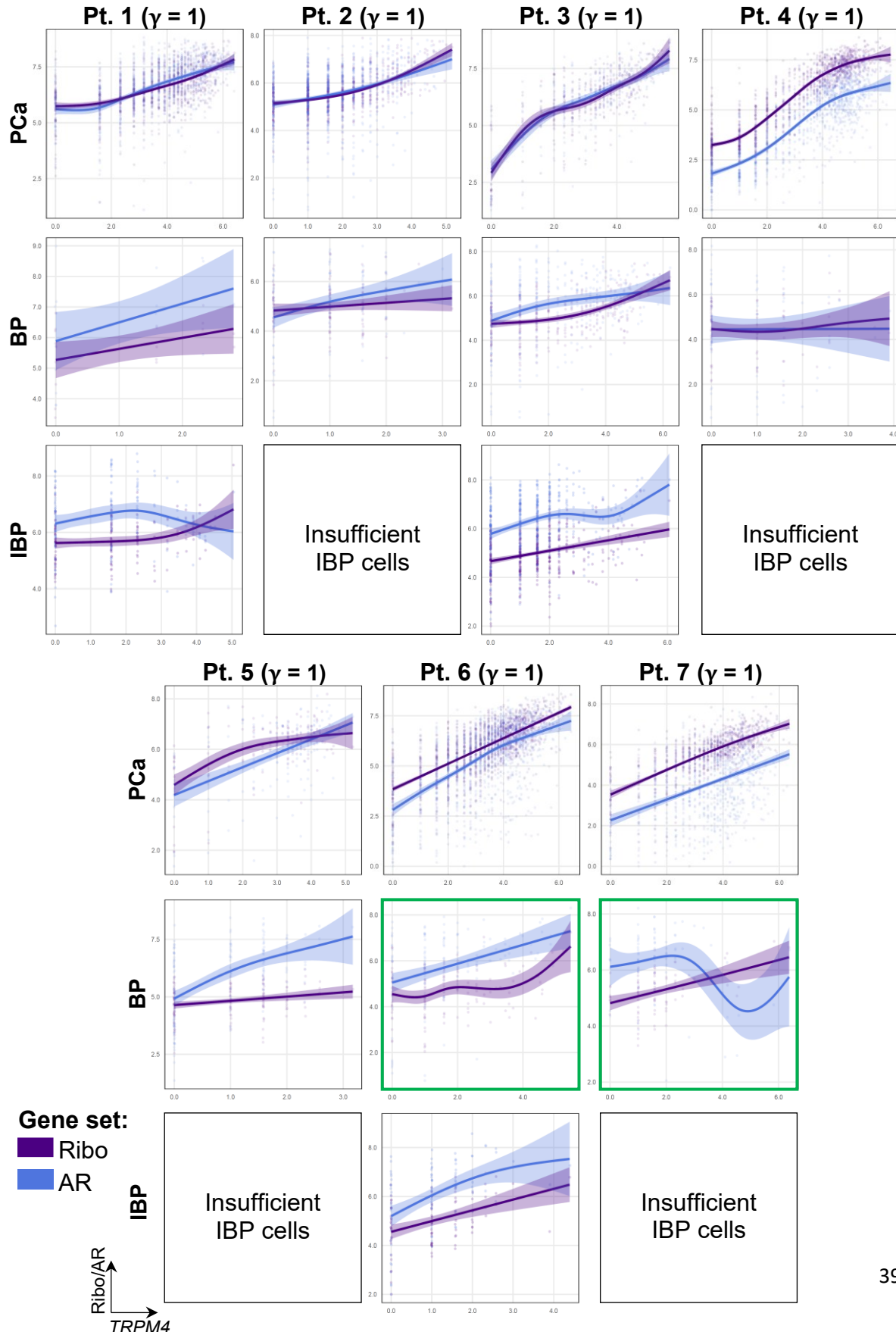
*Note: Supplementary Tables 1 to 13 (Excel format) are available on Zenodo:
<https://zenodo.org/records/17114394>*

Supplementary Figure 1



Supplementary Figure 1. The `gam.check()` plots of *TRPM4*-Ribo and *TRPM4*-AR modeling to assess if the data distribution was appropriate for Gaussian GAM analysis. Four types of plots were generated *i.e.*, Q-Q plot (top left), histogram of deviance residuals (top right), residuals versus fitted values (bottom left), and response versus fitted values (bottom right).

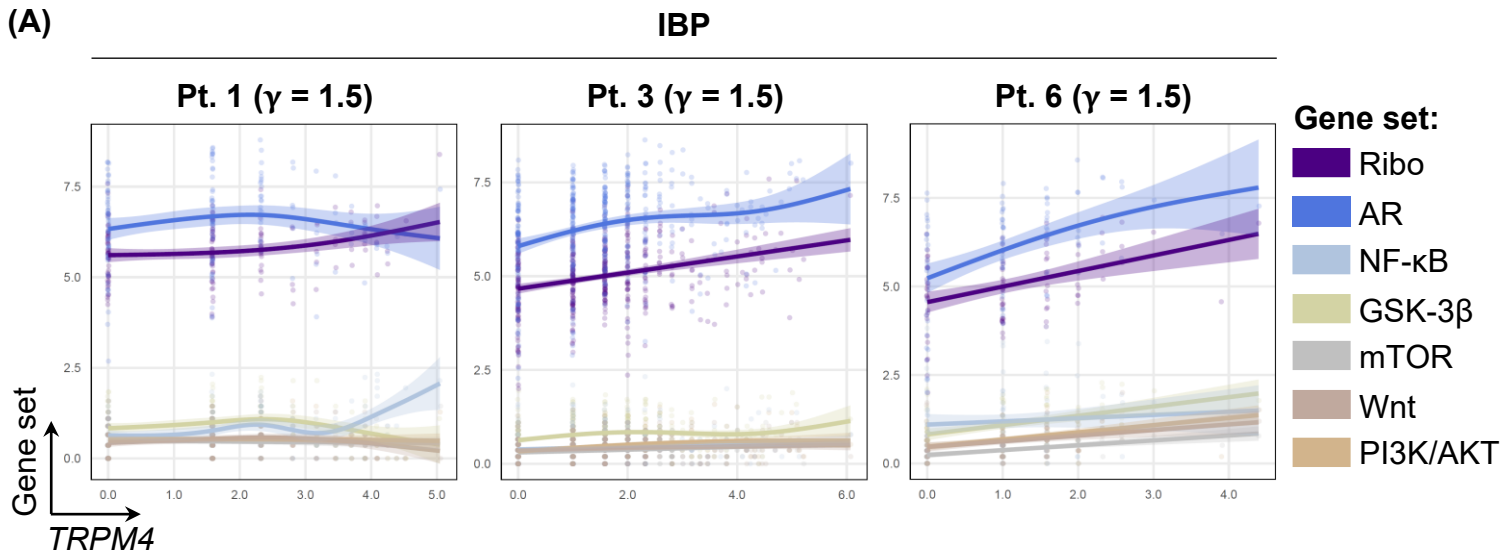
Supplementary Figure 2



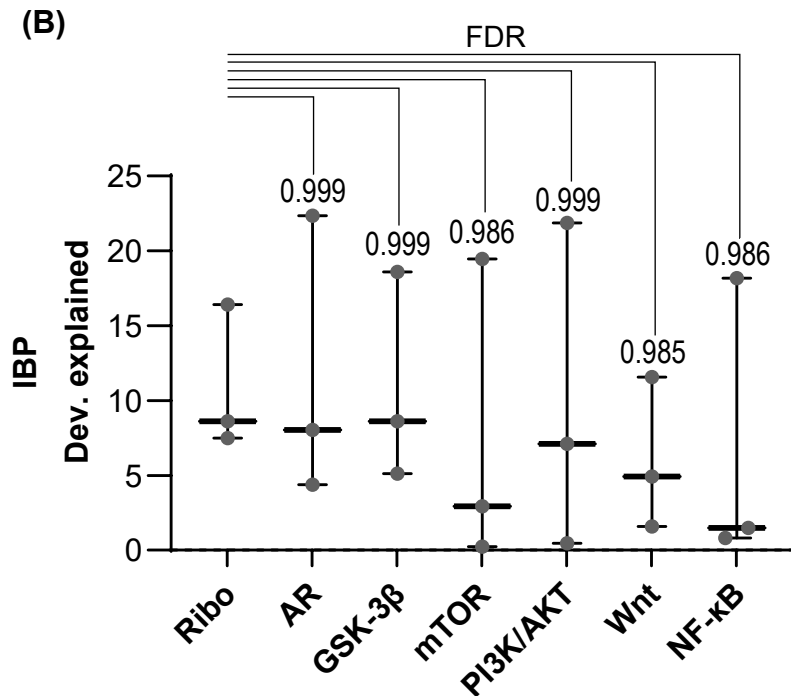
Supplementary Figure 2. GAM plots of *TRPM4*-Ribo and *TRPM4*-AR modeling in PCa, BP, and IBP cells, using the default γ value of 1 by mgcv.

Supplementary Figure 3

(A)



(B)



Supplementary Figure 3. *TRPM4*-gene sets modeling in IBP cells (A) GAM plots of *TRPM4* with multiple gene sets modeling in IBP cells ($\gamma=1.5$); (B) Comparison of DE between different gene sets modeling with *TRPM4* in IBP cells, and DE values from each gene set modeling were compared with DE of *TRPM4*-Ribo modeling.